UNIVERSIDADE DE LISBOA
FACULDADE DE CIÊNCIAS
DEPARTAMENTO DE FÍSICA

Automatic selection of multiple response functions for Generalized Richardson-Lucy spherical deconvolution of diffusion MRI data

João Carlos Holbeche Fino da Costa Gabriel

Mestrado Integrado em Engenharia Biomédica e Biofísica
Perfil em Sinais e Imagens Médicas

Dissertação orientada por:
Alexandre Andrade, PhD, Faculdade de Ciências da Universidade de Lisboa, Portugal
Alexander Leemans, PhD, University Medical Center, Utrecht, Netherlands

2021

“You become strong by defying defeat and by turning loss and failure into success.”

- Napoleon Bonaparte

Acknowledgements

Over the 6 months of this traineeship, I could not be more thankful to Prof. Alexander Leemans for hosting me at the University Medical Center, Image Sciences Institute in Utrecht, Netherlands, allowing me to have this fantastic opportunity.

A very special thank you to Alberto De Luca for his constant guidance and support throughout this project, his academic knowledge and attention were an inspiration for me.

To everyone at the University Medical Center, especially from the Image Sciences Institute, from whom I learned constantly and created such a welcoming and pleasant work environment, I will always be grateful for the time spent there.

A special thanks to the Erasmus + fund which was crucial for funding my stay in the Netherlands and made this internship possible.

I would like to thank my internal supervisor Prof. Alexandre Andrade, for all the guidance during the traineeship as well as throughout the last six years of the integrated BSc/MSc in Biomedical Engineering and Biophysics in Faculdade de Ciências da Universidade de Lisboa.

Thanks to all my friends and colleagues, who in different ways have helped this journey. A special thank you to Sousa and Neto for all the moments shared over the past 6 years, from studying together to going to the Netherlands, and more importantly for the strong relationship we have built over both happy and (very) stressful moments. To Beatriz and Bia, for also going to the Netherlands and making the stay even more fun, you, together with Sousa and Neto, made me feel at home even though we were away. I am sure we will nourish our friendship from wherever we are. I would also like to thank Inês, for giving me her precious notes that helped me a lot while studying this course. Thank you to one of my oldest friends, Plamen, for his advice and for being the best friend and housemate over the past six years. Beatriz, thank you for being my best friend, I am grateful for having such an amazing and caring person like you in my life. Thank you for being my partner in crime, for our endless laughs, inspiring conversations, and for always supporting and encouraging me.

Lastly, I would not forget my family, the most important people in my life. I cannot thank enough my parents who provided the means to make this traineeship possible, for always being by my side and for all the patience and encouragement along the years.

These six months in the Netherlands were not always easy, but in the end, it was one of the best experiences I could have asked for both academically and personally, and it would not have been possible without the support of all the people mentioned above.

Abstract

To understand the development of the human brain, more detailed information is required regarding the structural and functional cerebral organization and maturation. This development is the product of a complex series of dynamic and adaptive processes, and one of the best ways to understand it is through the study of the neonatal brain. The neonatal brain is not fully developed as it would be expected, so it goes through many changes regarding brain size, vasculature, and cognition.

Constrained spherical deconvolution (CSD) is a widely used approach to quantify the fiber orientation distribution (FOD) from diffusion magnetic resonance imaging (dMRI) data of the brain, which allows the reconstruction of more complex white matter (WM) bundles *in vivo*, including in neonates. However, this method estimates the response function (RF) based on the model of a single fiber population and uses it to try to reconstruct the local WM orientations.

Since the brain has a complex tissue organization, multiple tissues must be considered. It is not appropriate to use a WM RF throughout the whole brain because this can lead to spurious fiber orientation reconstructions and bad performance during fiber tractography. By accounting for multiple tissues, properties of grey matter (GM) and cerebrospinal fluid (CSF) can be captured, and partial volume effects (PVE) reduced. The acquisition of more comprehensive high-resolution multi-shell dMRI data offers opportunities to take into account multiple tissue types. Ultimately, these improve fiber tractography and consequently lead to a better understanding of the human brain and its development.

The generalized Richardson-Lucy (GRL) method can overcome these challenges by performing robust spherical deconvolution (SD) and suppress spurious FOD peaks on multi-shell dMRI data due to PVE. However, in the GRL method, three tissue classes are typically pre-defined to represent WM, GM, and CSF, using fractional anisotropy (FA) and mean diffusivity (MD) values taken from literature. These two metrics are derived from the diffusion tensor model (DTI), with FA measuring how anisotropic is the tensor in each voxel and MD measuring the average of the diffusion rate at each voxel.

This study aims to develop a method that automatically determines the number of tissue types (classes) that are needed to properly perform GRL in each analyzed brain dataset. The dataset used in this work consists of ten neonates and ten adults from the Developing Human Connectome Project (dHCP) and the Human Connectome Project (HCP), respectively.

The first part of this study consisted of developing a method for the automatic detection of the number of tissue types in the brain, by applying a gaussian mixture model (GMM) and the Bayesian information criterion (BIC) to automatically extract the number of tissue classes from the histogram of dMRI properties. In the second part, the GRL method was applied to the data to estimate the RF of each tissue that was automatically chosen in the first part, and therefore calculate the FOD and perform fiber tractography. This approach was designated by “GRL-auto”. Lastly, a comparison between the basic GRL formulation and GRL-auto was done. Since GRL uses predefined values calibrated on HCP data, it becomes clear that small differences were expected on such dataset, whereas on dHCP larger differences were expected.

Our analysis showed that our method automatically identified three classes in the FA histogram and two classes in the MD histogram when using HCP and dHCP data. Therefore, these results demonstrated consistency regarding the FA and MD values and their respective number of selected classes, for both datasets. Furthermore, different stages of WM maturation were detected in the dHCP data, but also some imperfections around the ventricles and crossing fibers areas. All FA and MD spatial maps were in line with anatomical correspondence and were consistent across all neonatal and adult subjects, demonstrating the efficiency of this method. The values of the WM, GM, and CSF fraction maps were plausible, in line with

the expected anatomy, and looked consistent on both HCP and dHCP datasets. The signal fraction maps determined with the HCP data showed almost no difference between GRL and GRL-auto. However, in the dHCP data, we observed notable differences, particularly in the GM and CSF maps. Regarding the FOD estimation, our results showed no difference in the HCP data. Nevertheless, for the dHCP data, GRL-auto estimated high-quality FODs in WM, and detected more peaks in crossing fiber regions and a bigger angular difference between the main FOD peaks, as compared to GRL. Lastly, we showed that GRL-auto led to improvements in fiber tractography, which will likely support gaining a better understanding of the human brain and its development.

Therefore, we can conclude that the method developed in this study is efficient and consistent in the automatic selection of the number of tissues needed to properly perform GRL in a brain, given multi-shell data, which was the main goal.

Key-words: neonatal, diffusion magnetic resonance imaging, generalized Richardson-Lucy, fiber tractography, brain development.

Resumo

O processo de desenvolvimento do cérebro humano tem sido objeto de estudo desde há vários anos, levando a avanços significativos no que diz respeito à compreensão das suas diferentes fases e mecanismos. Visto que este desenvolvimento resulta de uma série de complexos processos dinâmicos e adaptativos, existe uma busca contínua de informação sobre a sua organização estrutural e funcional, bem como o seu processo de maturação.

A ressonância magnética de difusão (dMRI) é uma técnica bastante completa no que diz respeito à análise do cérebro *in vivo*. Esta técnica é utilizada para realizar um mapeamento quantitativo, através da aplicação de modelos como o modelo de difusão tensorial (DTI). Estes modelos fornecem medidas que caracterizam o cérebro, tais como a anisotropia fraccional (FA) e difusividade média (MD), permitindo assim a quantificação de microestruturas e consequentemente a reconstrução de feixes de substância branca (WM) que ligam diferentes regiões cerebrais. Dadas as suas propriedades de difusão anisotrópica e a sua constituição fibrosa, as fibras de WM têm sido amplamente estudadas através da dMRI. Além disso, a tractografia tornou-se a abordagem padrão no que diz respeito à avaliação da conectividade cerebral usando dados de dMRI.

Os métodos de desconvolução esférica (SD) estão entre os mais utilizados para quantificar a distribuição da orientação das fibras (FOD) a partir de dados dMRI do cérebro, sendo que a forma mais comum de o fazer é com desconvolução esférica limitada (CSD). A ideia original da CSD baseia-se no facto de podermos escolher uma função de resposta (RF) representativa de um determinado tecido presente no cérebro e aplicar a SD para resolver o problema de cruzamento de fibras que o modelo de DTI não consegue resolver.

Uma vez que o cérebro possui uma complexa organização de tecidos, múltiplos tecidos devem ser considerados. Não é apropriado usar uma RF de WM em todo o cérebro, pois isso pode levar a reconstruções imprecisas da orientação das fibras e a um mau desempenho durante o processo de tractografia. Ao ter em conta múltiplos tecidos, as propriedades da substância cinzenta (GM) e do líquido céfalo-raquidiano (CSF) podem ser quantificadas, e os efeitos de volume parcial (PVE) podem ser reduzidos. Nos últimos anos, tem sido possível adquirir dados "multi-camada" mais complexos e de elevada resolução, mesmo em recém-nascidos, o que permitiu melhorar a técnica de CSD. Consequentemente, esta aquisição também vai melhorar a reconstrução da FOD no cérebro adulto, pois considera os PVE entre diferentes tipos de tecidos.

No cérebro neonatal existem algumas diferenças, pois este é constituído por WM em diferentes fases de maturação, e a GM possui características diferentes em comparação com um cérebro adulto. A possibilidade de distinguir diferentes tipos de fibras apenas com base nas suas características microestruturais deve-se às diferenças presentes no cérebro enquanto este se encontra numa fase de desenvolvimento. Em cérebros adultos, é menos provável conseguir observar tais diferenças.

Uma das melhores formas de compreender e estudar estes processos de desenvolvimento cerebral é através do estudo do cérebro de neonatais. Como seria de esperar, o cérebro de um recém-nascido não se encontra completamente maturado, sofrendo por isso diversas alterações até estar totalmente desenvolvido. Estas mudanças vão desde o aumento do tamanho do cérebro a alterações ao nível vascular, levando consequentemente a uma alteração dos processos de cognitivos. Em última análise, a aplicação de CSD a dados de "multi-camada" leva a uma extração mais precisa da FOD que por sua vez irá melhorar o processo de tractografia e levará, consequentemente, a uma melhor compreensão do cérebro humano e do seu desenvolvimento, particularmente se aplicada em recém-nascidos e comparada com adultos.

O método *Generalized Richardson-Lucy* (GRL) pode superar os problemas encontrados pela CSD através da realização de SD robusta, suprimindo picos imprecisos na FOD em dados "multi-camada" de dMRI. Este método pode definir múltiplos tecidos que irão aumentar a precisão da estimativa da FOD. No entanto, no método GRL, as três classes de tecidos representadas (WM, GM e CSF) são pré-definidas com valores FA e MD retirados da literatura.

Este estudo consistiu em desenvolver um método que determina automaticamente o número de classes (tecidos) necessárias para aplicar corretamente GRL no cérebro com dados "multi-camada", utilizando para isso os seus valores de FA e MD. O objetivo é aplicar corretamente o método de GRL no cérebro com as classes obtidas, de forma avaliar se existe uma melhoria no processo de estimação das FOD e por sua vez no processo de tractografia. Os dados utilizados neste trabalho consistem em dados de dMRI de dez neonatais e dez adultos, fornecidos pelo *Developing Human Connectome Project* (dHCP) e pelo *Human Connectome Project* (HCP), respetivamente. Estes dados já se encontravam num formato pré-processado, pelo que não foi necessário realizar qualquer etapa adicional neste sentido.

A primeira parte do estudo consistiu no desenvolvimento do método de deteção automática do número de tipos de tecidos no cérebro. Para isso, todos os dados foram processados no ExploreDTI, um programa de interface gráfica para dados de dMRI e que permite, por exemplo, a realização de tractografia. Este programa foi também usado para extrair os valores de FA e MD dos dados de dMRI dos cérebros dos neonatais e dos adultos, de modo a analisar a sua distribuição de valores por todo o cérebro através de histogramas. De seguida foi aplicado um *gaussian mixture model* (GMM) aos histogramas de FA e MD, utilizando o MATLAB R2018a, de forma a decompor os dados em classes. Depois de aplicar o GMM aos dados, foi determinado o número ideal de Gaussianas para os mapas de FA e MD. Para isso foi calculado o *Bayesian information criterion* (BIC) de cada modelo, em que cada um destes se caracteriza por um certo número de Gaussianas. De seguida, foi calculada a probabilidade do valor de cada voxel pertencer a uma das classes escolhidas de FA e MD, atribuiu-se assim uma classe a cada voxel. Posteriormente selecionaram-se as três melhores combinações de FA e MD de cada classe com base na frequência de ocorrência de cada combinação, sendo que cada classe foi definida pela média e desvio padrão das respetivas Gaussianas. Por fim, foram criados mapas espaciais do cérebro com as classes finais, utilizando o MATLAB R2018a.

Na segunda parte do estudo aplicou-se o método GRL aos dados, de forma a estimar a RF de cada um dos tecidos que foram selecionados na primeira parte. Estas duas partes do trabalho integram a nossa abordagem, sendo esta designada por "GRL-auto". No método GRL, a RF da GM e do CSF é baseada em valores de FA e MD retirados da literatura, enquanto que o método GRL-auto desenvolvido neste estudo estima esses valores através da seleção automática dos valores de FA e MD que são característicos de cada um destes tecidos. Obtiveram-se os mapas das frações de sinal da WM, GM, e CSF e foram feitas comparações entre o método GRL e GRL-auto. As FOD da WM obtidas com ambos os métodos foram comparadas entre si em regiões de cruzamento de fibras, tanto para neonatais como para os adultos. Por fim, para ambos os métodos, procedeu-se à tractografia em neonatais.

Os resultados indicam que, tanto para recém-nascidos como para adultos, existe consistência em relação aos valores de FA e MD e ao seu respetivo número de classes selecionadas. Além disso, conseguem ser observadas diferentes fases de maturação de WM nos neonatais, mas também algumas imperfeições à volta dos ventrículos e regiões onde ocorre cruzamento de fibras. Todos os mapas espaciais de FA e MD fizeram sentido anatomicamente, sendo consistentes quer nos neonatais quer nos adultos, demonstrando assim a eficácia deste método. Os mapas de sinal das frações de WM, GM, e CSF apresentaram valores plausíveis e concordância com a anatomia esperada, para além de consistência tanto nos recém-nascidos como nos adultos. Os mapas de frações de sinal dos adultos praticamente não apresentaram diferenças entre

os dois métodos. No entanto, os neonatais mostraram algumas diferenças notáveis, particularmente nos mapas de GM e CSF. Os resultados relativos às FODs não mostraram diferenças significativas no que diz respeito aos adultos. No entanto, para os neonatais, o método GRL-auto estimou FODs de elevada qualidade na WM, em comparação com o método GRL. Além disso, o método GRL-auto detetou mais picos plausíveis em regiões de cruzamento de fibras par além de uma diferença angular maior entre os principais picos das FOD, em comparação com o método GRL. Por fim, este método demonstrou uma melhoria no processo de tractografia, o que por sua vez levará a uma melhor compreensão do cérebro humano e do seu desenvolvimento.

Conclui-se assim que o método desenvolvido neste estudo é eficiente e mostra consistência no que diz respeito ao processo de seleção automática do número de tecidos necessários para efetuar CSD no cérebro. Observou-se uma melhoria na tractografia das fibras, o que permitirá uma melhor compreensão da maturação do cérebro bem como das conexões entre as diversas regiões, tendo-se, assim, cumprido o objetivo principal deste trabalho.

Palavras-chave: neonatais, ressonância magnética de difusão, Richardson-Lucy generalizado, tractografia, desenvolvimento cerebral.

Table of Contents

List of Figures

List of Tables

List of Abbreviations

ADC - Apparent Diffusion Coefficient
AFD - Apparent Fiber Density
BIC – Bayesian Information Criterion
CSD - Constrained Spherical Deconvolution
CSF – Cerebrospinal Fluid
CT - Computed Tomography
DTI - Diffusion Tensor Imaging
DW – Diffusion Weighted
DWI - Diffusion-Weighted Imaging
FA - Fractional Anisotropy
FOD - Fiber Orientation Distribution
GM – Grey Matter
GMM - Gaussian Mixture Model
GRL - Generalized Richardson-Lucy
HARDI - High Angular Resolution Diffusion Imaging
HCP - Human Connectome Project
MD – Mean Diffusivity
MRI - Magnetic Resonance Imaging
MS-CSD - Multi-shell Constrained Spherical Deconvolution
MSMT-CSD - Multi-shell Multi-tissue Constrained Spherical Deconvolution
PGSE - Pulsed-Gradient Spin-Echo
PVE - Partial Volume Effects
RF - Response Function
SD – Spherical Deconvolution
SE - Spin Echo
SH – Spherical Harmonics
SNR - Signal-to-noise Ratio
SSST-CSD - Single-shell Single-tissue Constrained Spherical Deconvolution
WM - White Matter
dRL - Damped Richardson-Lucy
dHCP - Developing Human Connectome Project
dMRI – Diffusion Magnetic Resonance Imaging

1. Introduction

Magnetic Resonance Imaging (MRI) is a non-invasive technique that allows imaging of the human body without the need for ionizing radiation which is instead used in x-rays and computed tomography (CT). MRI is based on the interaction of spins with electromagnetic fields and has become one of the standard non-invasive non-ionizing imaging modalities.

Structural and functional imaging have benefited from MRI applications such as diffusion-weighted imaging (DWI). This technique relies on the random microscopic motion of water molecules to study the underlying microstructure of tissues [1]. Diffusion Magnetic Resonance Imaging (dMRI) is a very comprehensive technique to analyze the brain *in vivo*. It can be used for quantitative mapping, through the application of models such as diffusion tensor imaging (DTI), which provide metrics that characterize the brain [2]–[5]. It can also be used to reconstruct the white matter (WM) bundles that connect different brain regions.

Given its anisotropic diffusion properties and its fibrous constitution, WM tracts have been widely studied with DWI [6], providing good contrast to images. Numerous metrics can be extracted from DWI data to quantify these microstructures. Moreover, tractography has become the standard approach to assess brain connectivity using diffusion data [7].

Making use of dMRI data, spherical deconvolution (SD) methods are the preferred way to model the fiber orientation distribution (FOD). The most common way to do this is with constrained spherical deconvolution (CSD), a method that was introduced in 2004 [8]–[10]. The original CSD idea is based on the fact that we can take a response function (RF) that is representative of a single fiber population and apply spherical deconvolution to solve the crossing fibers problem of DTI.

The problem is that CSD can only estimate high-quality FODs in voxels containing WM. By having other tissue types present, such as grey matter (GM) and and cerebrospinal fluid (CSF), the RF will no longer be appropriate and therefore CSD will estimate unreliable FODs [11]. However, in recent years, it has been possible to acquire more complex high-resolution multi-shell data, even in neonates, to make the CSD technique better.

This makes it possible to investigate the validity of classic dogmas in SD. In the adult brain, it has been shown that acquiring multi-shell dMRI data allows improving the FOD reconstruction by considering partial volume effects (PVE) between different tissue types. This is more challenging in the neonatal brain because it consists of WM at different maturation stages, and GM tissue is different than in adults.

To overcome these challenges, the generalized Richardson-Lucy (GRL) method was introduced [12]. This method can perform robust SD and suppress spurious FOD peaks on multi-shell dMRI data. This alongside the definition of several tissue classes can increase the accuracy of the FOD estimation. The problem is that these tissue types are defined arbitrarily. One way to solve this is by assuming that we have three tissues in the brain, WM, GM, and CSF. Although the existing methods have been optimized for adults to account for these three tissues, their functioning will likely be suboptimal in neonates and infants, since the brain structure is still in maturation. This also does not work if there is a disease affecting the brain because that pathology “class” is not represented in the tissue types.

With this work we aim to devise a method that automatically determines the number of tissue types (classes) that are needed to properly perform GRL in a brain, based on their fractional anisotropy (FA) and mean diffusivity (MD) values, given multi-shell data. This method has been designated as “GRL-auto”. The

data used in this project was provided by the Developing Human Connectome Project (dHCP) and the Human Connectome Project (HCP) [13].

This project is part of the integrated BSc/MSc in Biomedical and Biophysics Engineering of Faculdade de Ciências da Universidade de Lisboa in Portugal and took place at the University Medical Center in Utrecht, the Netherlands, from September 2019 to February 2020.

This thesis is divided into six chapters. Theoretical background on dMRI principles is described in Section 2.1. DTI fundamentals are explained in Section 2.2 and RF are briefly reported in Section 2.3. spherical harmonics (SH) basics are mentioned in Section 2.4 and SD principles and applications are reported in section 2.5. A description of CSD is shown in Section 2.5.1 and 'multi-shell, multi-tissue constrained spherical deconvolution' is presented in Section 2.5.2, as well as a comparison with 'single-shell, single-tissue constrained spherical deconvolution'. Furthermore, the GRL method is introduced in Section 2.5.3. Section 2.6 describes the tractography technique and its relationship with the above-mentioned sections. Sections 2.7 and 2.8 explain the clinical relevance of this project and the type of information neonatal data can provide in dMRI and its limitations, respectively. Section 2.9 explains the limitations of the above-mentioned methods.

The study dataset is described in Section 3.1, including a description of the dMRI data acquisition. Section 3.2 explains the process of automatic detection of the number of tissue types present in the brain. This includes how FA and MD were obtained as well as the implementation of the gaussian mixture model and the Bayesian information criterion. The application of GRL to the selected classes is fully described in Section 3.3. This includes the resampling of the data and the implementation of the GRL method. Section 3.4 describes the analysis made to compare the GRL and GRL-auto.

The results regarding the tissue type selection are reported in Section 4.1, including FA and MD histograms in Section 4.1.1, class selection in Section 4.1.2. and spatial maps with the chosen classes in Section 4.1.3. The results of the application of GRL with the optimized classes (GRL-auto) are presented in Section 4.2, with signal fraction maps displayed in Section 4.2.1, FODs in Section 4.2.2, and tractography results in Section 4.2.3. The discussion of these results is in Section 5 and the final remarks are shown in Section 6.

2. Theoretical Background

2.1. Diffusion Magnetic Resonance Imaging

2.1.1. Principles of Diffusion

Diffusion MRI is a type of MRI technique that is sensitive to the random microscopic motion of water molecules. A detailed explanation of MRI is beyond the scope of this work but it can be found in reference [14]. In physics, this random microscopic motion of water molecules is called Brownian Motion, or simply Diffusion. Einstein described this diffusion with the well-known equation,

$$\langle x^2 \rangle = 2Dt_d \tag{2.1}$$

where $\langle x^2 \rangle$ (m^2) is the mean-squared displacement of the particle during a diffusion time t_d (s) and D $(m^2 \cdot s^{-1})$ is the diffusion coefficient [15].

The human body consists mostly of water, and water molecules are always interacting with various tissues and exchanging between the intracellular and extracellular environments. Therefore, Eq. 2.1 cannot be applied since diffusion is not considered to be free. In neuronal tissues, the water in the extracellular space is characterized by hindered diffusion [16]. This type of diffusion has a Gaussian displacement pattern, where the diffusion coefficient is reduced. This leads to a replacement of the D term in Eq. 2.1 by the apparent diffusion coefficient (ADC) for each measured direction. On the other hand, the water in the intracellular space is described by restricted diffusion. The displacement in this type of diffusion is characterized by a non-Gaussian distribution, which does not obey Eq. 2.1.

2.1.2. Imaging

The spin-echo (SE) sequence is an MRI sequence with a 90-degree radiofrequency pulse, followed by a 180-degree pulse, allowing to cancel the effects of local inhomogeneities. Diffusion encoding is based on the pulsed-gradient spin-echo (PGSE) sequence, which consists of applying two identical diffusion-weighted (DW) gradient pulses inserted before and after the refocusing pulse of a conventional SE sequence [17] (Figure 2.1).

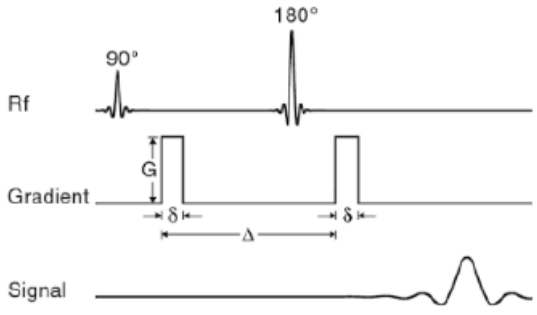

***Figure 2.1**: Schematic representation of a PGSE sequence. G is the amplitude of the magnetic field gradients. The time between the onset of the two gradient pulses is represented by Δ and the gradient pulse duration by δ. Picture from* [23].

After the 90-degree radiofrequency pulse, a magnetic field gradient pulse is applied to the sample for a short time, which will cause the spins to acquire a phase based on their position at the time of the pulse application. The 180-degree pulse is then applied to reverse the phase of the spins, followed by another identical gradient pulse which changes the phase of the spins based on their position at the time of the second pulse. If no diffusion has occurred, the phase acquired from the second pulse will be equal and opposite to the phase of the spin just before the pulse, resulting in a net phase of zero. However, if diffusion occurs, the mean squared phase of all spins will not be zero leading to a loss in the MR signal, which can be measured and used to calculate the ADC.

The degree of diffusion weighting is characterized by the strength and timing of the gradients used to generate the diffusion images and is usually called *b*-value (s/mm^2). This can be given by the expression below,

$$b = \gamma^2 \delta^2 |G|^2 \left(\Delta - \frac{\delta}{3}\right) \tag{2.2}$$

where γ $(s^{-1} \cdot T^{-1})$ is the gyromagnetic ratio of the nucleus, $G(T \cdot m^{-1})$ is the amplitude of the magnetic field gradients, δ (s) their duration, and $\Delta(s)$ the time interval between them [18]. According to Eq. 2.1, the attenuation of the MR signal due to diffusion can be expressed as,

$$\frac{S}{S_0} = exp(-bD) \tag{2.3}$$

where S and S_0 are the signal intensities measured in the presence and absence of the diffusion gradients, respectively.

When the water diffuses equally in all directions, the ADC is the same regardless of direction, which suggests an isotropic diffusion. On the contrary, anisotropic diffusion is the process when the water molecules preferentially diffuse according to certain directions, leading to alterations in the ADC. In WM the diffusion is anisotropic, whereas in GM and CSF the diffusion is isotropic [19]. In WM there are axons and water diffuses preferentially along the main axis. In GM, despite the existing cell bodies being considered as "barriers" to the diffusion process, water still diffuses isotropically. However, this occurs at a lower rate when compared to CSF, since in CSF there is almost free diffusion.

2.2. Diffusion Tensor Imaging

Reconstruction algorithms model the water molecules rearrangement distribution, thus allowing to determine the principal direction of WM fibers. They also provide information about the microstructure of the biological tissues and are used in fiber tracking.

DTI is an MRI-based neuroimaging technique that can estimate some properties of diffusion in large WM tracts [20]. From this model, we can extract helpful parameters, such as the FA, MD, and the orientation of the major eigenvector of the diffusion tensor, which indicates the fibers' direction [21]. This tensor defines the magnitude, the degree of anisotropy, and orientation of the water diffusion, and can be mathematically represented by a 3x3 symmetric matrix like the one below.

$$D = \begin{bmatrix} D_{xx} & D_{yx} & D_{zx} \\ D_{xy} & D_{yy} & D_{zy} \\ D_{xz} & D_{yz} & D_{zz} \end{bmatrix} \tag{2.4}$$

This diffusion tensor can be represented by an ellipsoid (Figure 2.2) that shows the probability of the molecules disposition due to the diffusion. The main axes are given by the eigenvectors of the ellipsoid, and their diffusion displacements by the square root of the eigenvalues.

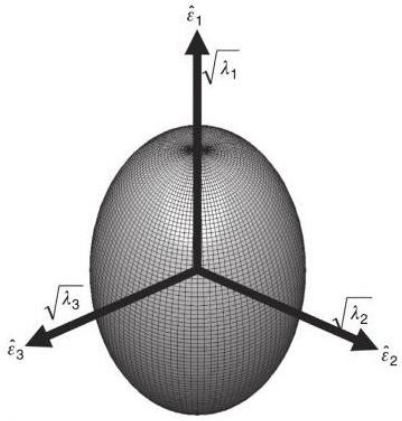

Figure 2.2*: Abstract visualization of the diffusion tensor. The principal axes of diffusion are given by the eigenvectors, $\hat{\varepsilon_1}$, $\hat{\varepsilon_2}$ and $\hat{\varepsilon_3}$, and their respective diffusion displacements over a given diffusion time given by the square root of the eigenvalues λ_1, λ_2 and λ_3. Picture from* [23].

This vector can be color-coded, yielding cartography of the tracts' position, direction (red for right-left, blue for foot-head, green for anterior-posterior), and anisotropy (as indicated by the tract's brightness) [22].

Due to the symmetry in the diffusion process, the DT only requires a minimum of six DW images to estimate the elements of the tensor and one non-DW image [23]. The higher the number of images the better is the precision of this technique, and usually the optimal number is 30 [24]. However, it is not easy to interpret the DT data. The two main properties that can be inferred from DTI analysis are the FA and the MD. The FA measures how anisotropic is the tensor in each voxel, estimating the main direction of the diffusion [25].

$$FA = \sqrt{\frac{3}{2}} \frac{\sqrt{(\lambda_1 - MD)^2 + (\lambda_2 - MD)^2 + (\lambda_3 - MD)^2}}{\sqrt{{\lambda_1}^2 + {\lambda_2}^2 + {\lambda_3}^2}} \tag{2.5}$$

FA values vary from 0 to 1, with higher values reflecting increased directionality of diffusion, whereas lower values indicate that diffusion is nearly the same in all directions, regardless of the magnitude of diffusion.

The MD is defined by the average of the eigenvalues, measuring the average of the diffusion rate at each voxel, making assumptions about the diffusion type and the geometry of the tissue microstructure. The MD can be given by Eq. 2.6.

$$MD = \frac{\lambda_1 + \lambda_2 + \lambda_3}{3} \tag{2.6}$$

Making assumptions based on these DTI parameters requires some precaution since the measured diffusion effects are averaged over a voxel (millimetric scale) in comparison to the size of individual axons (micrometric scale). Although FA is usually associated with WM integrity, we must take into account the fact that changes in myelination, increase in extracellular/intracellular water, cell death and fiber orientation will change the FA values [15].

The extent to which the image is weighted by diffusion is controlled by the b-value. Therefore, when the b-value equals zero, the images are not weighted by diffusion, and when the b-value is greater than zero (e.g. b=1000 s/mm^2), the images are DW.

In voxels where there is no diffusion, the spins acquire random phases, leading to a signal loss. This explains the black appearance of the ventricles on DW images. When the diffusion is hindered, the signal is higher, leading to the gray appearance of the brain parenchyma on DW images.

In the brain, WM includes tightly packed bundles of neuronal axons [20]. With dMRI it is possible to gather specific information about these WM fiber pathways, noninvasively.

Nonetheless, this model has some limitations [2], mostly because it lies on the presumption of unhindered diffusion, thus is only an approximation for *in vivo* cases. Also, the DT has a single main orientation [3], so it cannot describe properly a system that has more than a single oriented fiber population in a certain region (Figure 2.3) [4]. It is known that one-third of white matter voxels contain more than one fiber population [5], thus being affected by this problem [26].

The current dMRI feasible resolutions lead to a large number of voxels that will not be well described by this model [4]. Furthermore, the orientation of the fibers cannot be accurately estimated, which will lead to unreliable results when performing tractography techniques that rely on the diffusion tensor model [27].

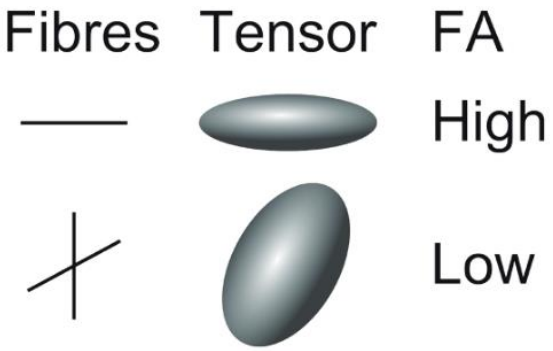

Figure 2.3: *The problem with crossing fibers in DTI. With a single fiber population, the diffusion tensor is an ellipsoid and FA is high. With two fibers crossing, the diffusion tensor becomes more spherical resulting in a reduced FA. Picture from* [15].

2.3. Response Function

The DW signal attenuation measured from one fiber population can be represented by an axially symmetric RF, R(θ), where θ is the elevation angle in spherical coordinates.

For more than one fiber, the signal S(θ, ϕ) (ϕ is the azimuthal angle in spherical coordinates) can be given by the convolution over the unit sphere of the RF R(θ) with a fiber orientation density function F(θ, ϕ), as given in Eq. 2.7.

$$S(\theta, \phi) = F(\theta, \phi) \otimes R(\theta) \tag{2.7}$$

The FOD gives the portion of fibers within the sample that are aligned along the direction (θ, ϕ), therefore containing all the volume fraction information. In the case of having N fibers, the FOD is just the sum of N Dirac delta functions along the direction of each fiber population and weighted by their respective volume fractions.

F(θ, ϕ) can be obtained by performing the spherical deconvolution of R(θ) from S(θ, ϕ) if R(θ) is already known (Figure 2.4). When estimating the volume fractions, the number of fiber populations must be known and each of these fiber populations must have a single orientation. Therefore, this technique cannot be applied to *in vivo* cases.

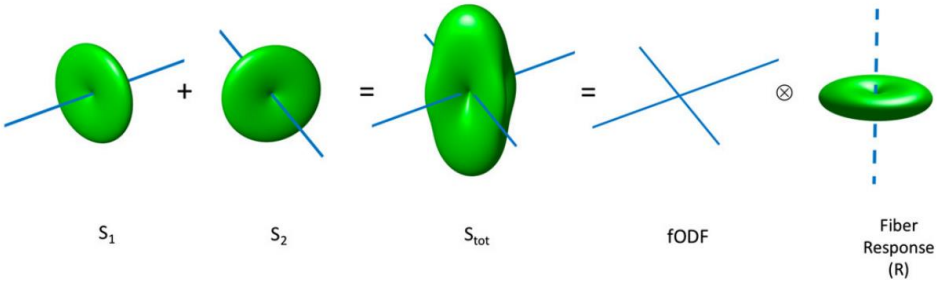

Figure 2.4: *Illustration of the SD approach. Picture from* [28].

In the study of F. Dell'Acqua *et al.* [28], simulations showed that using inaccurate RFs only affects the estimated volume fractions of the different fiber populations, and not their respective orientations. It can also be seen from the results of this work [28] that the effect of low SNR on the DW signals does not appear to have a significant impact on the reliability of SD.

2.4. Spherical Harmonics

SH are basis functions to represent signals lying on the unit sphere that can be described by two numbers: the harmonic degree L ($L \geq 0$) and order M ($-L \leq M \leq L$) (Figure 2.5). The angular frequency is directly proportional to L.

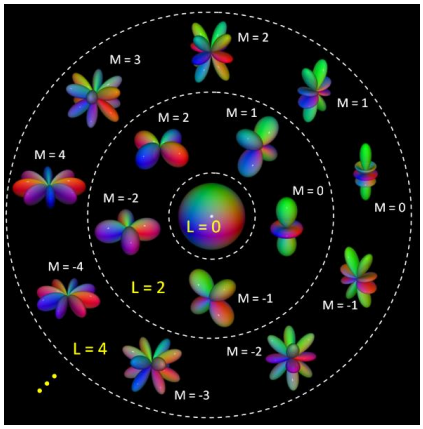

Figure 2.5: *SH representation regarding the degree L and order M. Image courtesy by Alexander Leemans.*

The SD operation can be formulated as the action of an ensemble of rotations on a function defined over a sphere [29]. The representation of S(θ, ϕ) regarding the nth order is given by Eq. 2.8:

$$\underline{S}^n = R\,\underline{F}^n \tag{2.8}$$

The SD operation can therefore be reduced to a simple set of matrix multiplications and can be achieved by inverting each R^n matrix to recover $\underline{F}^n$. Since R(θ) has axial symmetry, the R^n collapses down to a single real scalar constant. The SH representation of S(θ, ϕ) can be obtained by using a simple linear least squares fit [4]. The FOD can then be estimated using SD as described above, assuming that R^n can be estimated.

The angular resolution will increase with higher diffusion weightings (b-values), however, the signal attenuation is so large that the noise begins to dominate, leading to a decrease in the signal-to-noise ratio (SNR). Intermediate b-values produce better results because they introduce the strong angular dependence necessary to resolve the fiber orientations, without attenuating the signal down to the noise level [30].

The use of high order harmonics makes the SD technique increasingly sensitive to noise, but able to resolve smaller angular resolution. Optimal results would be obtained using a high SNR, high spatial resolution, high angular resolution data acquisition, using a fairly high b-value dependent on the actual SNR of the images [30].

As stated above, the main assumption inherent in SD is that the RF measured for a typical coherently oriented fiber population is constant throughout the brain. However, this may not be true in regions where the WM fibers have significantly different diffusion characteristics, such as myelination levels and axonal diameters or densities [31].

Where there is a regional variation in these parameters, the RF used to perform SD may not accurately reflect the diffusion properties of the fiber tracts. However, it is important to note that using an inaccurate

RF only affects the estimated volume fractions of the various fiber populations, not their respective orientations [30].

2.5. Spherical Deconvolution

SD is a fast computational method that only uses linear operations, thus its noise propagation characteristics can be inferred very easily. The assumption that the diffusion characteristics of all fiber populations found in the brain are identical is made. Therefore, all variations in diffusion anisotropy are assumed to be associated with PVE [30].

The DW signal arising from different regions is assumed to add independently to generate the total measured signal, therefore, the DW signal can be approximated as the sum of signals with distinct orientations on the unit sphere.

There are a few models that can provide information about WM fiber pathways, such as multiple tensor fitting and Q-ball imaging. However, each of these has inherent limitations. Previous work [30] showed that SD can reconstruct the original FOD adequately from a dataset acquired on a standard clinical scanner, without imposing any *a priori* information about the number of fiber populations present in a voxel. Optimal results can be obtained by using a high b-value, high SNR, high spatial resolution, and high angular resolution, as it has been shown [30]. It was showed that SD failed to resolve fiber populations whose orientations were too close [30]. Moreover, the SD technique is limited by a number of harmonic orders, which will influence the maximum angular resolution that can be achieved.

There are two main families that use this technique: one is CSD alongside with multi-shell CSD, and the other is GRL. Both techniques are presented below, but in this work we focus on GRL.

2.5.1. Constrained Spherical Deconvolution

Noise introduces spurious negative lobes in the reconstructed FOD, which are not physically possible. Instead of filtering out the high angular frequencies, another way of decreasing the ill-conditioning of SD is by adding a non-negativity constraint on the presence of these negative values in the FOD [8].

CSD is an iterative method that preserves the angular resolution in SD while maintaining noise robustness. Firstly, the fiber RF is estimated directly from the DW data, then the DW signals are reoriented to assure that their principal axes of diffusion are aligned. At last, the RF SH coefficients are estimated from the single fiber DW signals and the matrix relating the coefficients of the FOD to the DW signal can be calculated analytically [30]. Ultimately the crossing fibers problem can be solved by extracting the coefficients of the FODs.

CSD can resolve fiber orientations that are separated by small angles, which improves the accuracy of tracking results for tracts that pass through or close to other tracts that are similarly oriented. High b-values emphasize the difference in the DW signal attenuation which will generate a ‘flatter’ RF. Therefore, SD performs better in the presence of crossing fibers when the b-values are higher. Moreover, with CSD it is possible to apply SD to data that was probably intended to use in diffusion tensor analyses, and therefore has low b-values and/or number of DW directions.

As stated above, this technique improves angular resolution and fiber orientation assessment [32], [33] which is very helpful in tractography since it relies on accurate estimates of the WM FODs [8]. Furthermore, the sharper the peaks in the FOD the better the spatial localization of the connectivity maps generated will be [9], [10].

As shown in a study by J. D. Tournier *et al.* [8], the CSD method can significantly improve the robustness of SD, and consequently of the estimated fiber orientations. The precision of the estimated peak orientations was found to be dependent on the angle separating the two fiber populations [8], and is highest when the two fiber orientations are maximally separated, and drops as it becomes more difficult to resolve the two orientations. The data used in the mentioned study showed that higher b-values resolved better the crossing fibers, as stated above. However, it was also demonstrated that it is possible to use lower b-values, which were previously believed to be inappropriate.

2.6.1.1. b-value and directions effect

Besides noise, using high b-values can lead to problems with image pre-processing, especially regarding eddy-currents and motion correction. However, there are now methods that can easily use this data and still get good results [34], [35].

The b-value influences the angular frequency of the DW signal. The signal changes from being perfectly isotropic at b = 0 s/mm^2 to a flatter shape as the b-value increases (Figures 2.6 and 2.7). Therefore, while a minimum of 28 DW directions might be sufficient at b = 1000 s/mm^2, at b = 3000 s/mm^2 is required at least 45 DW directions [36]. The higher the number of directions the better the overall SNR of the reconstruction will be [21].

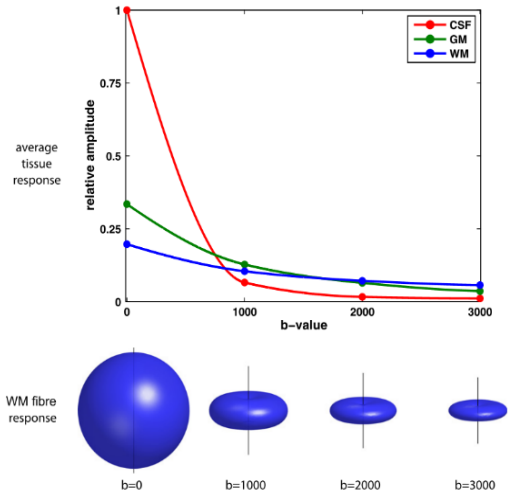

Figure 2.6: *b-value effect on the average tissue response (top) and on the WM fiber response (bottom). Picture from* [40].

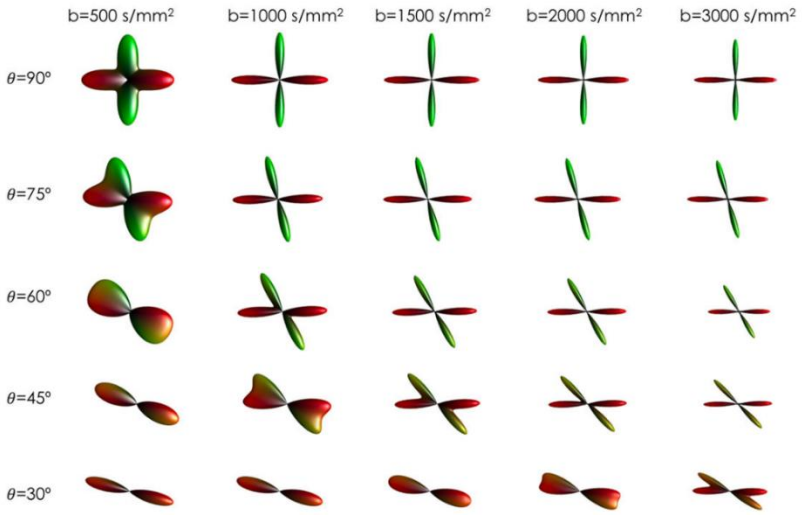

Figure 2.7: *Effect of different b-values on FOD reconstruction. Picture from* [28].

2.5.2. Multi-shell constrained spherical deconvolution

Fiber tractography allows local fiber orientation estimation, which will help deduce the pathways connecting distant regions of the brain [37], [38]. Apparent fiber density (AFD) is a quantitative measure derived from the FOD. AFD measurements are proportional to the intra-axonal water volume fraction and can be linked with a single fiber population within a voxel containing multiple fiber populations [39].

The CSD method is mainly designed for data acquired with a single diffusion weighting, also known as 'single-shell, single-tissue CSD' (SSST-CSD) [40]. CSD can produce high-quality FOD estimates in voxels containing pure WM. However, in voxels containing GM and CSF, the single fiber RF is no longer accurate [11], [42].

With the 'multi-shell, multi-tissue CSD' (MSMT-CSD) technique, various b-values are used, allowing estimation of different RF for each b-value and tissue type, which will lead to better results when performing tractography (Figure 2.8) [40]. The MSMT-CSD method can be considered non-parametric since it only imposes a certain degree of spherical smoothness to the FODs and does not lean on a specific mathematical model for each tissue, but instead estimates a tissue RF directly from the data [40].

B. Jeurissen *et al.* [40] demonstrated that the SSST-CSD method overestimates the WM volume in voxels that contain CSF and GM. Since the FOD amplitude scales linearly with the WM volume fraction, this will distort the AFD measures. However, MSMT-CSD can eliminate almost completely this effect, which significantly improves AFD's accuracy. Moreover, considering GM and CSF PVE, the precision of the FOD fiber orientations improves significantly when changing from SSST-CSD to MSMT-CSD, since most-spurious peaks that might lead to angular biases are efficiently removed [40]. This benefits tractography since the increased precision and reduced number of spurious peaks result in less noisy tractograms where WM interacts with GM and CSF [40].

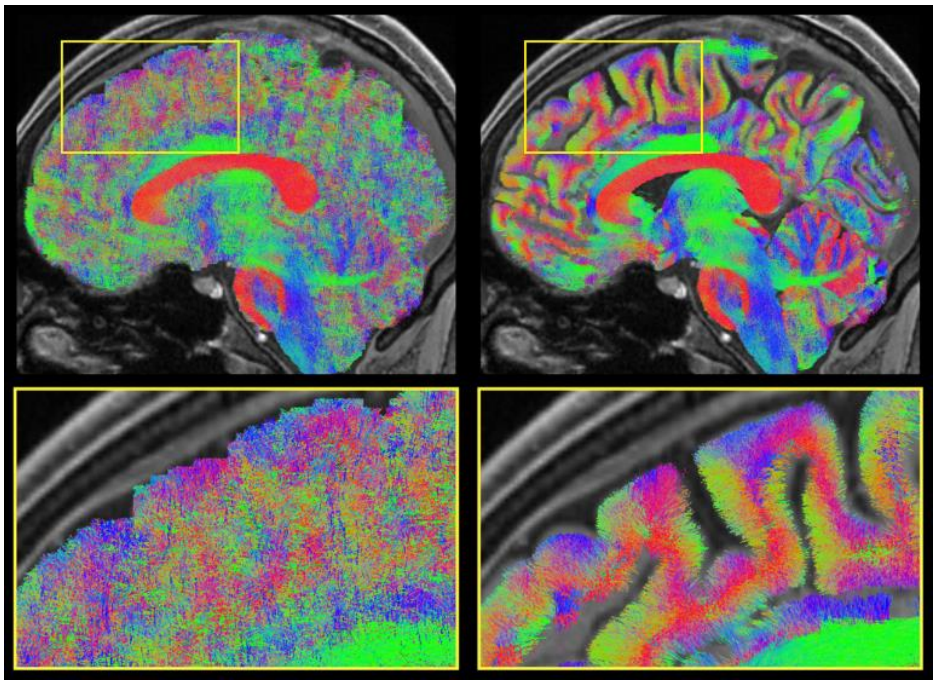

Figure 2.8: *Sagittal visualisation of a fiber tractogram obtained from WM FODs estimated with SSST-CSD (left) and MSMT-CSD (right). Picture from* [40].

When using SSST-CSD for fiber tracking, large FOD amplitude thresholds are needed to avoid tracking into CSF and isotropic GM. However, with MSMT-CSD, it is possible to use much lower FOD thresholds without resulting in spurious tracts. This allows MSMT- CSD's to detect very small WM structures that would be thresholded out if fiber tracking was performed using SSST-CSD [40].

MSMT-CSD can perform segmentation of WM, GM, and CSF in the brain directly from the DW data without using any previous spatial information. Although the estimation is only voxel-wise, the segmentation is very similar to the anatomical [40]. Moreover, the GM and CSF volume fractions can be used as new quantitative metrics, just like the FOD is used for the AFD of WM fibers [39], [42].

2.5.3. Richardson-Lucy spherical deconvolution

Richardson-Lucy SD is a method that estimates the FOD from single-shell dMRI data [43]. This framework can avoid artifacts that may derive from the SH representation, by extracting the FODs directly from the signal domain [12]. This approach also requires the definition of a deconvolution matrix *H*, which contains the RFs of each tissue, and converts the dMRI signals into SH, which leads to the FODs. The FOD of each voxel can be estimated by Eq. 2.9,

$$\left[FOD^{(k+1)}\right]_i = \left[FOD^{(k)}\right]_i \frac{[H^T s]_i}{\left[H^T H \cdot FOD^{(k)}\right]_i} \tag{2.9}$$

where $FOD^{(k)}$ is the expected FOD at the *k*-th iteration along the *i*-th direction sampled on the unit sphere of SH, *H* is the *m* by *n* matrix that maps *m* measured signals into *n* directions, and H^T is the transpose of *H*.

Later on, this method was adapted to increase the robustness of the FOD estimation to PVE in isotropic tissues by Dell'Acqua *et al*. [11], leading to the damped Richardson-Lucy (dRL) method. This method extends Eq. 2.9 by adding a term that attenuates the overestimation of the FODs to noise or isotropic classes [12].

The GRL is a method based on the dRL algorithm that was introduced by Guo *et al*. [12]. The GRL uses SD to improve the accuracy of the WM FODs by accounting for an arbitrary number of tissue classes defined by the user [12]. While the dRL can perform robust SD and suppress spurious FOD peaks only on single-shell dMRI data, GRL can use multi-shell dMRI data alongside the definition of several tissue classes to increase the accuracy of the FODs. Furthermore, the GRL can estimate the signal fraction maps according to the number of tissue classes and then use these maps to terminate the fiber tractography process, especially at the WM/GM interface or at the outer GM surface, which results in a more accurate tractography [12]. When creating the deconvolution kernel *H*, Guo *et al*. consider WM, GM, and CSF as the three represented tissue types, and this matrix can be given by Eq. 3.9, where *p* is the number of shells.

$$H_{GRL} = \begin{bmatrix} H_{dRL,1,WM} & H_{dRL,1,GM} & H_{dRL,1,CSF} \\ \vdots & \vdots & \vdots \\ H_{dRL,p,WM} & H_{dRL,p,GM} & H_{dRL,p,CSF} \end{bmatrix} \tag{2.10}$$

2.6. Fiber tractography

Parametric approaches produce estimates of several parameters such as the orientations and volume fractions, whereas the non-parametric approaches give estimates of a continuous distribution of orientations such as the FOD [28].

The FOD can get accurate results for single and multiple fiber populations by directly modeling or deconvolving the angular blurring introduced by the diffusion process, recovering more information of the fiber orientation (Figure 2.9) [21]. To get precise results in tractography, the characterization of the FOD is extremely important since the estimated parameters are used for further processing [7], [12], [26], [44]–[46]. Since there is an important interaction between microstructural parameters, such as the fiber density, and the FOD, the FOD must be estimated as precisely as possible [39], [42].

The fiber orientation information can be represented in a continuous or discrete way. The continuous distribution has the advantage of being more general, which leads to the opportunity of representing any given arrangement of fiber orientations a voxel [47], [48]. It also has the advantage of linearity with the signal, leading to reconstruction times of the order of seconds to minutes for typical whole-brain dataset. SH are commonly used in these type of representations [4], [30], [41], [49]–[54].

Another way to represent the fiber orientation information is through a discrete set of fiber populations. This is referred to as fixels, a fiber population within a voxel [55], [56]. Each fixel is usually represented by some parameters such as orientation and volume fraction, and the number of fixels per voxels is generally assumed to be low [26], [57]–[59].

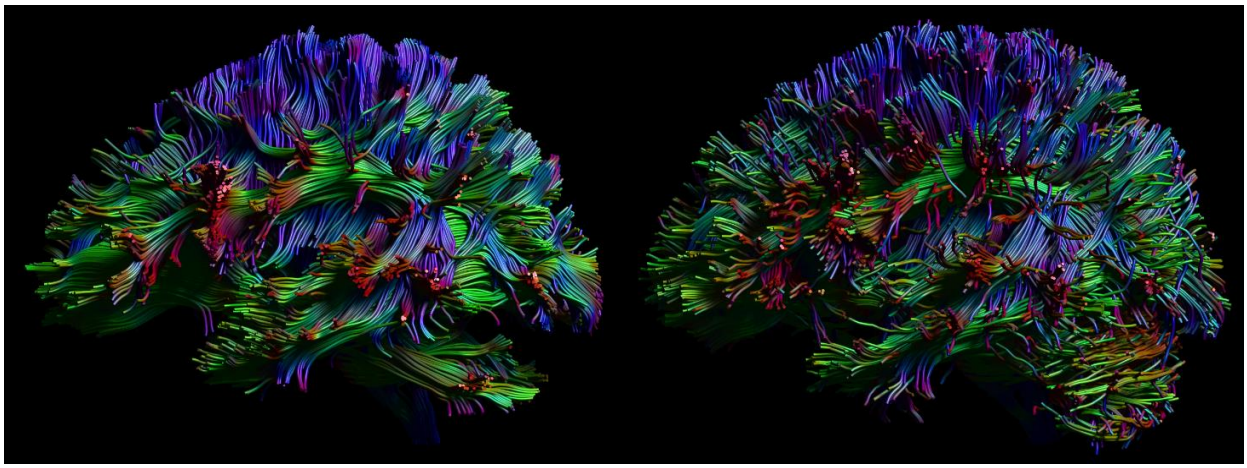

Figure 2.9: *Whole brain tractography using DTI (left) and CSD (right). Image courtesy by Alexander Leemans.*

However, the relationship between fiber orientations and the signal is not linear which leads to long reconstruction times. Moreover, these methods will consistently favor simpler models if the data is very noisy, by assuming a single fiber population when more may be present. This will lead to biased results and the estimated orientations will not be correct, which has obvious implications in tractography.

Tensor model-based approaches are easy to implement and have been shown to give a very close approximation to more complex fiber response models based [42]. If a model-based fiber response is well-

calibrated, not only it has a satisfactory performance [60] but also, in some SD applications, it can be used to adjust the balance between angular resolution and noise stability of the recovered FOD [11], [43].

In SD methods, the RF may not be constant throughout the whole brain. For instance, it has been shown that WM tracts have differences in their axonal diameter distributions, which will affect the corresponding diffusion signal [21]. However, assuming a constant fiber RF can be relatively beneficial, since the problem then remains linear and can be solved solidly and effectively. Furthermore, because axial and radial diffusivities change, this will not have a big impact on the shape of the RF, but more in scale and amplitude [61]. The estimate of the fiber density will be incorrect, but the orientation estimate will be mostly unaltered [30], [42].

If a well-defined RF is used, it will lead to a reduction in the FOD amplitude, and consequently to a reduction in fiber density. In recent works where SD is used, it has been found that in WM, the microstructural anisotropy is very similar and uniform throughout the brain, thus supporting the validity of assuming a constant RF [62]. Furthermore, some methods can estimate an RF for each voxel, which is a very complex problem to solve since the FOD and the RF are strongly related [49], [63].

2.7. Clinical Relevance

WM consists essentially of bundles of myelinated nerve fibers (axon). These nerve fibers are long extensions of nerve cells (neurons) that connect specific brain regions. These fibers are tightly packed together into fiber bundles, which share a common origin and destination. The full map of brain connections is often called the connectome [64], [65].

The use of fiber tractography in neuroscience is extremely important due to the ability of this technique to define non-invasively the WM fiber pathways in the brain. This has become the main process to investigate quantitative MRI parameters in WM bundles. Fiber tractography is extremely beneficial for neurosurgeons, who want to have a better assessment when planning a surgery, but also very important in "connectomics," a technique that studies and creates maps of the complex network of the brain [66].

Fiber tracking is a complicated process since it involves a lot of steps that lead to an accumulation of errors. These errors will lead to false positives/negatives and biased connections in the "connectomes", due to the complexity of the underlying fiber bundle structure. Therefore, it is crucial to be aware of these underlying steps and the corresponding errors, since these will greatly influence the fiber tractograms [66].

However, tractography has provided remarkable results regarding large WM structures that could not be obtained by any other *in vivo* imaging technique. Applying real anatomical priors and ensuring that the tractograms match the data will lead to a much better biological accuracy, thus useful connectivity information can be obtained. Nonetheless, even when using state-of-the-art techniques and high-quality data, many problems that could eventually bias the "connectomes" remain unresolved, which leaves room for improvement [66].

2.8. dMRI in the neonatal period

The neonatal period corresponds to the time interval between birth and twenty-eight days of life. During this period, the brain goes through many changes, such as increasing its size [67] and changing in density, cellular composition, and water content [68]. To better understand how the brain develops, more information is needed regarding the proliferation, migration, and maturation of the cells. However, the acquisition, processing and analysis of neonatal diffusion data is very difficult, since this modality is sensitive to patient motion and low SNR [69].

The FOD-based analysis using CSD [8] allows the definition of more complex WM bundles in neonates [70]. However, this analysis does not take the temporal evolution of the WM signal into account. Relaxation-based neonatal atlases are very important because they allow high-resolution anatomical maps with contrast sensitivity to the changes that occur during the development of the brain [69]. DWI provides complementary information about microstructural tissue properties, which are very important when characterizing developments in neonatal brains [71]. Moreover, diffusion atlases may provide information regarding the orientation of the microstructures of the individual fiber populations and can assess the organization and microscopic properties of the fiber bundles.

High order diffusion model-based atlases overcome some of the limitations of diffusion tensor-based atlases. However, there are only a few atlases of the neonatal brain using high angular resolution diffusion imaging (HARDI) data. Tissues such as WM and GM are more difficult to break down into biologically meaningful components in neonatal data, in comparison to adult HARDI data [69]. The fact that it is possible to resolve different types of fibers based only on their distinct microstructural signature is due to the major differences present in the brain while it is developing. In adult brains, such differences are improbable to be observed [69].

A study by M. Pietsch *et al.* was done to establish a framework to help in the group-level and longitudinal analysis of WM regions or tracts of interest, using dMRI in neonatal [69]. This was accomplished by using components that were derived from the data itself instead of being modeled after biological tissue properties. Although it may not provide the same level of biological specificity that other explicit microstructure models provide, the previously mentioned work relies on a few assumptions and uses tissue-specific RF's instead of biophysical model quantities. For CSF, an isotropic RF was acquired. For WM, two anisotropic RF's were acquired in two different periods to simulate the temporal evolution of the signal due to the changing volume fractions [69]. Furthermore, multiple fiber populations within the same voxel were able to be resolved. Moreover, in some crossing fiber regions, different fiber bundles are attributed to different anisotropic responses, potentially expressing different stages of tissue maturation [69].

Since the two anisotropic WM response functions used correspond to two different ages, it is crucial to understand that both RF's will be naturally dependent on those ages. However, by using these two anisotropic RF's, fiber populations from different components in the same voxel can be directly resolved [69].

2.9. Limitations

As stated before, the tissue RFs are assumed to be the same in all voxels and the FOD response is also inferred to be the same for all fiber populations. However, the brain is made up of different cells, which have different sizes, densities, and permeabilities, which contribute to the violation of the previous assumption [40]. Nonetheless, this assumption is the same for all non-parametric SD approaches [72], since it is usually considered appropriate [44].

The GRL method also has limitations that should be acknowledged. This method, alongside with others [40], only accounts for the three main tissue types of the brain (WM, GM and CSF). Brain pathologies should also be taken into account, since they can change the structural MRI scan in a way that reliable tissue type identification is no longer feasible [40].

Instead of estimating the signal representation of each tissue type by using tissue masks like in other studies [40], in the GRL these estimations are made by using models with literature values in GRL [12]. The use of these predefined values has the advantage of not requiring any additional data and processing beyond the dMRI data. However, this choice can be inaccurate if changes in the chosen tissues occur. Furthermore, these literature values can only be applied to adult data where they are well known, which limits the application of GRL to neonatal data.

However, no study has investigated a method that automatically determines the number of tissue types of the brain, based on the FA and MD values extracted from the data itself, given dMRI multi-shell data. This new approach introduced in this study aims to properly perform GRL by using the tissue classes estimated automatically from the data, to obtain more accurate tissue RFs and consequently better FOD estimations and better tractography results.

3. Methods

3.1. Dataset

3.1.1. Subjects

The subjects of this study were ten infants that were recruited and imaged at the Evelina Newborn Imaging Centre, St. Thomas' Hospital, London, UK. All neonates of this study were imaged between 24-45 weeks of age and were also imaged in their natural sleep. If the baby woke up, scanning was halted, and attempts were made to resettle the subject without taking them out of the patient immobilization system. Even when sleeping peacefully, many babies moved and so all data were motion-corrected. In addition, ten healthy adults between 22-35 years of age were also included in this study to make a comparison with the infants. The data was provided by the dHCP and HCP, respectively [13].

3.1.2. Data acquisition

The dHCP data was acquired on a 3T Philips Achieva (running modified R3.2.2 software) using a dedicated neonatal imaging system that included a neonatal 32 channel phased array head coil [73]. A spherically optimized set of directions on four shells (b = 0 s/mm^2: 20; b = 400 s/mm^2: 64; b = 1000 s/mm^2: 88; b = 2600 s/mm^2: 128) [40] was split into four optimal subsets (one per Phase Encoding direction). These directions were then spread temporally taking motion and duty cycle considerations into account. If the baby woke up during the diffusion scan, the acquisition could be halted and restarted (after resettling the subject) with a user-defined overlap in acquired diffusion weightings [74]. The acquired resolution was 1.5x1.5 mm, 3 mm slices with 1.5 mm overlap and a 3800 ms TR and 90ms TE.

The HCP data was acquired on the Connectome Skyra, which is a customized 3T Siemens Skyra platform with 100 mT/m gradients for diffusion encoding. Each dMRI session led to the acquisition of DW data that consisted of four shells (b=0 s/mm^2, b=1000 s/mm^2, b=2000 s/mm^2, and b=3000 s/mm2), with each one acquired once with right-to-left and left-to-right phase encoding polarities [75]. The diffusion directions were obtained using a toolbox available from INRIA [76] that returns uniformly distributed directions in multiple q-space shells (90 DW directions), except for the b=0 s/mm^2 shell (18 DW directions). A spin-echo echo planar imaging sequence was used for this acquisition, with a 5520 ms TR, 89.5 ms TE, 210x180 (RO x PE) FOV, 1.25 mm isotropic resolution.

The dMRI data of both dHCP and HCP was downloaded in its already pre-processed format, which did not require any additional step.

3.2. Automatic estimation of the number of tissue types

3.2.1. FA and MD extraction and distribution

In this project, all the data was processed in ExploreDTI [77], a graphical toolbox for dMRI and fiber tractography. From the four available shells in the DW data, only two were selected (b=0 s/mm^2, b=1000 s/mm^2), as well as the corresponding DW directions for both the dHCP and HCP data.

Since different tissue types will likely have different FA and MD, the values of these parameters for all the neonatal and adult brains were also extracted with ExploreDTI to analyze their distribution of values across the whole brain. To do this, we computed histograms for both the FA and MD maps containing all voxels across the brain and looked at their frequency distribution.

The model used to obtain the FA and MD maps in ExploreDTI was the DTI model. The reason why only two shells were selected was due to this model requirements, since it only works with limited DW data and the values of the other shells were too high and would lead to restriction effects that would bias the estimates. Moreover, above b=1000 s/mm^2 the contribution of CSF would not be visible in the histograms.

3.2.2. Gaussian Mixture Model

A mixture model is a probabilistic model that can distinguish different classes present in a given data, by representing the probability distribution of the measurements in that data. These models perform statistical assumptions about the properties of the different classes, based only on the information that is given by the data. Therefore, it is possible to identify different classes in the data without requiring prior information about a specific measurement.

The gaussian mixture model (GMM) is a parametric probability density function represented as a weighted sum of M component Gaussian densities, where each component is defined by its mean and covariance [78]. It can be given by the equation,

$$p(x \mid \lambda) = \sum_{i=1}^{M} w_i \, g(x \mid \mu_i, \Sigma_i) \tag{3.1}$$

where x is a *D*-dimensional continuous data vector (*i.e.* measurements), w_i, i = 1, . . . , M, are the mixture weights, and $g(x \mid \mu_i, \Sigma_i)$, i = 1, . . . , M, are the component Gaussian densities. Each component density is a *D*-variate Gaussian function of the form,

$$g(\mathrm{x} \mid \mu_i, \Sigma_i) = \frac{1}{(2\pi)^{D/2}|\Sigma_i|^{1/2}} \exp\left\{-\frac{1}{2}(\mathrm{x}-\mu_i)'\Sigma_i^{-1}(\mathrm{x}-\mu_i)\right\} \tag{3.2}$$

with mean vector μ_i and covariance matrix Σ_i. The mixture weights satisfy the constraint $\sum_{i=1}^{M} w_i = 1$.

To achieve better modeling, the GMM uses a discrete set of Gaussian functions, each one with a specific mean and covariance. Thus, the individual component densities can model underlying classes in the data [78].

Taking these characteristics into account, the GMM was applied to the FA and MD histograms, to decompose the data into classes (tissue types), using MATLAB R2018a. Furthermore, it was also relevant to understand if these maps could give information about the selected types of tissues present in the brain, *i.e.* if that information could be specific to each of the identified tissues.

3.2.3. Bayesian information criterion

After applying the GMM to the data, it was important to determine the ideal number of fitted Gaussians for the FA and MD maps. To do this, the Bayesian information criterion (BIC) was computed for each model, which was characterized by a certain number of Gaussians.

The BIC is a commonly used tool in model selection, mainly because of its computational simplicity and efficient performance [79]. The computation of the BIC is based on the log-likelihood [80], which measures the goodness of fit of a model and does not require prior information.

The basic principle is to describe how well the model fits a series of observations and to measure the difference between the observed and expected values of the model [79]. This method assigns a score to each model, and the best model is represented by the minimum BIC value [79]. The BIC can be given by the following equation:

$$\mathrm{BIC} = k\ln(n) - 2\ln\left(\hat{L}\right) \tag{3.3}$$

where n is the number of observations, k is the number of parameters and $\hat{L}$ is maximized value of the likelihood function of the model.

If the model errors are independent and uniformly distributed according to a normal distribution, the BIC can be given by equation (3.4), where the $-2\ln\left(\hat{L}\right)$ term is substituted by $n\ln\left(\widehat{\sigma_e^2}\right)$ and $\widehat{\sigma_e^2}$ is the error variance.

$$\mathrm{BIC} = n\ln\left(\widehat{\sigma_e^2}\right) + k\ln(n) \tag{3.4}$$

The number of parameters k (number of fitted Gaussians) of the studied models increased gradually, leading to a continuous decrease of BIC. Not being possible to find a minimum value for BIC to select the best models, a percentage of change between the BIC of each model was determined. A threshold of 1% was applied to select the best models for the FA and MD maps, using MATLAB R2018a. For this case, the percentage change can be given by Equation (3.5), where i is the model number.

$$\text{Percentage change } = \frac{\Delta BIC}{BIC_i} = \frac{BIC_{(i+1)} - BIC_i}{BIC_i} \times 100 \tag{3.5}$$

A number of classes based on the ideal number of gaussians were then created for the best FA and MD model (Figure 3.1). Each class represented a type of tissue, defined by the mean and standard deviation of each gaussian.

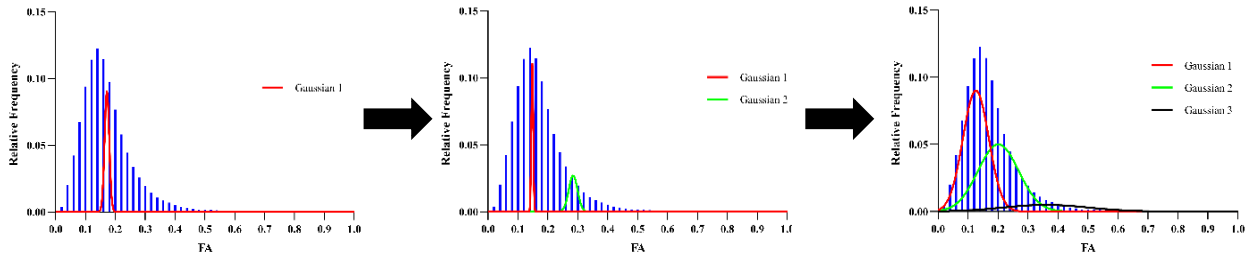

Figure 3.1: *Schematic representation of the iterative Gaussian fit process and selection of the best fit according to the BIC.*

The next step was to assign one of the selected classes to every voxel. For this, the probability of a voxel belonging to each one of the selected Gaussians was calculated for FA and MD.

Then, the three best combinations of the FA and MD classes were selected based on the frequency with which each combination occurred. The choice of three classes was conventional and not optimal, since the point was to represent the three main tissues of the brain (WM, GM and CSF). Every class was defined by the mean and standard deviation of the respective FA and MD Gaussians. Lastly, spatial maps of the brain with the final classes were created using MATLAB R2018a.

3.3. Performing spherical deconvolution with the optimized classes

3.3.1. Resampling

In this second part of the project, all four available shells in the DW data were used, as well as the corresponding DW directions for datasets. Because of its large size, the data was resampled to speed up the computation process. However, this resampling does not affect the results of this work. The resampling was performed in ExploreDTI, changing the resolution of the data to 2 mm isotropic.

Resampling data usually requires sampling between the centers of voxels using interpolation methods. The quality of the resampling result depends heavily on the quality of these interpolation methods. In ExploreDTI, the three available methods of interpolation for resampling are the *nearest neighbor*, *trilinear* and *B-spline*.

The *nearest neighbor* method is the simplest since it takes the value of the closest voxel to the desired point. Although this allows the preservation of the original voxel intensity, the final image will have much lower quality compared to the original. The *trilinear* interpolation is slower than the previous one and has led to the loss of high-frequency information from the image. Despite this, the final images have better quality than the ones acquired through the *nearest neighbor* method.

Finally, the *B-spline* method models an image as a linear combination of basis functions, in this case, B-spline functions. Before resampling the data, an image composed of coefficients is formed, thus involving a very fast deconvolution process [81], [82]. When resampling with this interpolation method, it is crucial to compute the right combination of basis functions for each point (local convolution). Since the images are initially transformed before applying local convolution, this interpolation method will lead to a much more efficient resampling [83]. Therefore, the interpolation method chosen to resample the data was the *B-spline.*

3.3.2. Application of GRL to the data

The GRL method requires the definition of several classes and how to define them. Considering the three main tissues in the brain (WM, GM and CSF), the definition of the RF of GM and CSF in the GRL method is based on FA and MD values taken from literature [12], whereas the WM RF is determined from the data itself (Section 2.6.3).

In this work we take GRL a step further by providing an automatic estimation of the optimal FA and MD values that represent each of these tissue types (Section 3.2). Therefore, the RFs present in the deconvolution matrix *H* of GRL will be defined with FA and MD values automatically estimated from the data itself. This approach will be addressed as “GRL-auto” (automatic class detection).

3.4. Analysis

The dHCP and HCP data were fit with GRL and GRL-auto using the above-described H-matrix (Section 3.3.2) to evaluate the effect on the fractional maps. The signal fractions estimated with GRL-auto were compared to those derived with GRL. The WM FODs obtained with GRL-auto were compared to those derived with GRL in crossing fiber regions, for both datasets. The number of peaks detected with GRL and GRL-auto were also analyzed, as well as the angular deviation between them. After visual inspection of the dHCP results, 0.1 and 0.3 were chosen as the peak threshold values for GRL and GRL-auto, respectively, where the peak threshold is considered the minimum amplitude of a "genuine" peak. The peak threshold for the HCP data was set to 0.1 for both methods. Lastly, whole brain deterministic fiber tractography was performed in ExploreDTI with the derived FODs for both GRL and GRL-auto on the dHCP dataset. This procedure was performed on both methods, using angle-threshold 30º, step size equal to half of the voxel-size, with seed points evenly sampled in the brain volume 2 mm^3 isotropic.

4. Results

4.1. Tissue types selection

This first part of the results concerns the automatic detection of the number of tissue types and is divided into three parts: (1) Presentation of the distribution of FA and MD values of the dHCP and HCP data through histograms; (2) The Gaussian fit of the FA and MD maps for both datasets, where these fits are represented in the histograms and their relationship with the BIC shown; (3) Spatial maps of the brain using the final assigned tissue types for FA and MD as well as the joint spatial map of FA and MD, where boxplots of these classes for both datasets are also presented.

4.1.1. FA and MD histograms

As described in Section 3.2.1, histograms were computed to have a visual inspection of the range and distribution of the FA and MD values in the brain of neonates and adults. For FA, the dHCP data showed a normal distribution of the values, varying approximately between 0.02 and 0.6. As can be seen in Figure 4.1, the FA frequency distribution is quite similar among all dHCP subjects. The MD values were between 0.0005 mm^2/s and 0.004 mm^2/s, and the respective histogram had a normal distribution with a long right tail. The MD frequency distribution was also very similar across all dHCP subjects. (Figure 4.2).

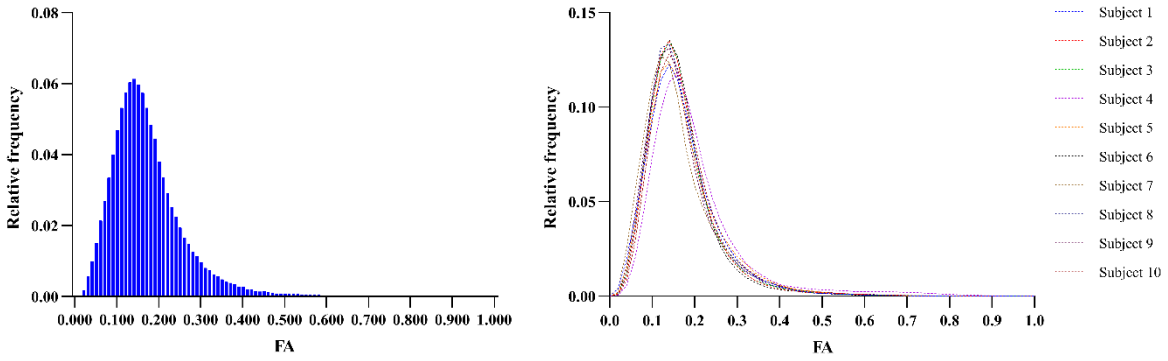

Figure 4.1: *Distribution of FA values for one dHCP subject (left) and for all dHCP subjects (right).*

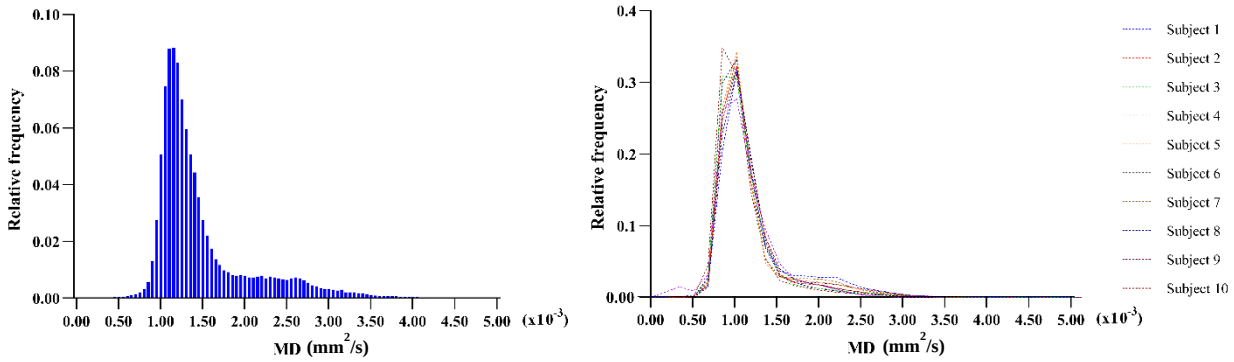

Figure 4.2: *Distribution of MD values for one dHCP subject (left) and for all dHCP subjects (right).*

Regarding the HCP data, FA histograms did not show a normal distribution of the values like the dHCP (Figure 4.3). Indeed, the values presented a wider interval, varying approximately between 0.02 and 0.9, and looked very similar among all subjects. The MD values of the HCP data were between 0.00045 mm^2/s and 0.003 mm^2/s, and the respective histogram had a normal distribution with a long right tail, very similar to the dHCP MD histogram, across all HCP subjects (Figure 4.4).

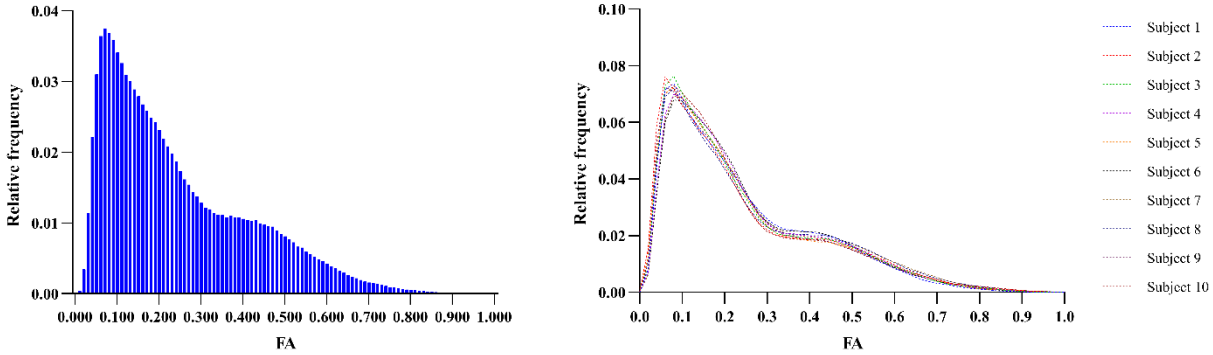

Figure 4.3: *Distribution of FA values for one HCP subject (left) and for all HCP subjects (right).*

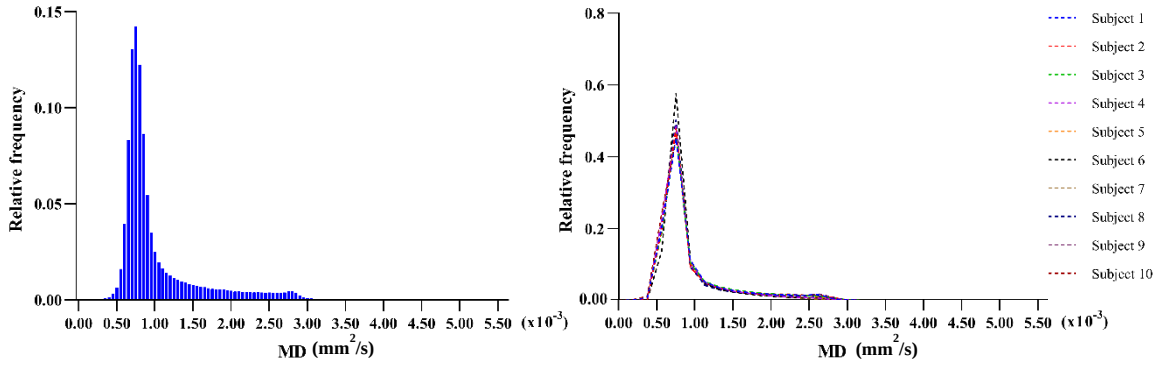

Figure 4.4: *Distribution of MD values for one HCP subject (left) and for all HCP subjects (right).*

4.1.2. Class selection

After applying the GMM to the dHCP and HCP data (Section 3.2.2), the optimal number of Gaussians was selected based on the BIC values of each model. The BIC of the first three models is shown in Table 4.1. The values decrease from one model to the next due to the increasing number of parameters, as would be expected.

To choose the best model for FA and MD, the percentage of change between the BIC of each model was calculated for a 1% threshold, as described in Section 3.2.3, and is shown in Table 4.2. Regarding the BIC values of the FA models, both datasets showed a higher difference from the first to the second model in comparison with the difference between the second to the third model. For MD, the difference between the BIC values of the second and third models was below the 1% threshold, therefore are not presented in Table 4.2. It can also be noticed that the differences between the FA and MD models were smaller for dHCP data than for HCP data.

Table 4.1: *BIC values of FA and MD for each gaussian model of all dHCP and HCP subjects.*

	BIC FA (Mean ± STD)			**BIC MD (Mean ± STD)**		
	1st Model	**2nd Model**	**3rd Model**	**1st Model**	**2nd Model**	**3rd Model**
Neonates	-3,82E+05 ± 4,92E+04	-4,57E+05 ± 5,09E+04	-4,65E+05 ± 5,22E+04	-2,45E+06 ± 2,92E+05	-2,61E+06 ± 3,22E+05	-2,62E+06 ± 3,22E+05
Adults	-4,34E+05 ± 7,78E+04	-7,15E+05 ± 9,18E+04	-7,68E+05 ± 9,77E+04	-9,02E+06 ± 1,06E+06	-9,99E+06 ± 1,17E+06	-1,00E+07 ± 1,18E+06

Table 4.2: *Change in percentage of the BIC values between each FA and MD model, for all dHCP and HCP subjects.*

	BIC FA change % (Mean ± STD)		**BIC MD change % (Mean ± STD)**
	1 - 2	**2 - 3**	**1 - 2**
Neonates	19.97 ± 8.52	1.78 ± 0.41	6.47 ± 1.55
Adults	65.97 ± 9.94	7.38 ± 0.98	10.72 ± 1.04

Tables 4.1 and 4.2 show that, for all dHCP and HCP subjects, the ideal number of Gaussians is three for FA and two for MD. Therefore, Gaussian fits with the corresponding number of classes of FA and MD were computed over the histograms of the neonates and adults (Figures 4.5 to 4.8).

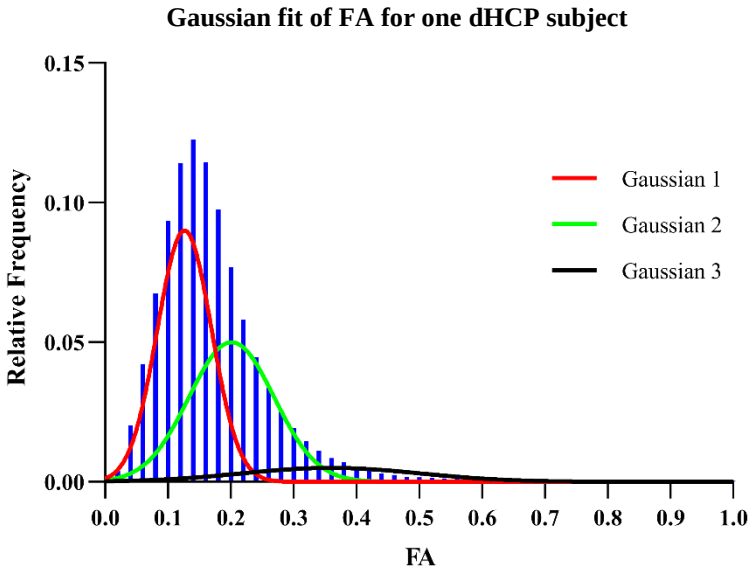

Figure 4.5: *Fit of the 3 selected gaussians to the FA histogram of one dHCP subject.*

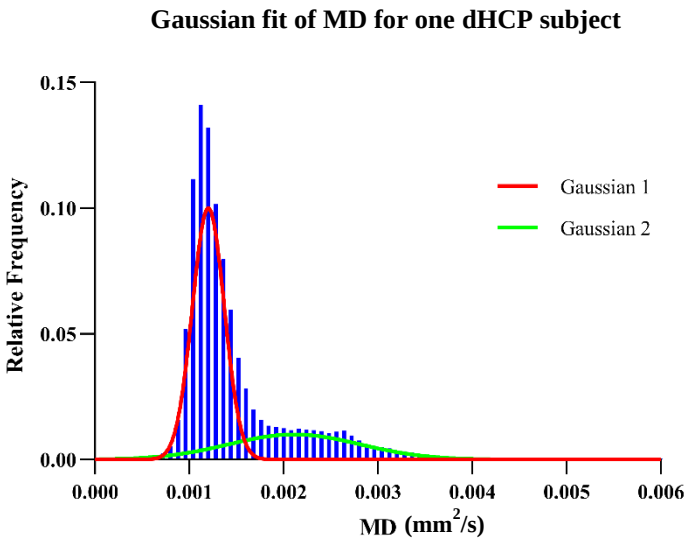

Figure 4.6: *Fit of the 2 selected gaussians to the MD histogram of one dHCP subject.*

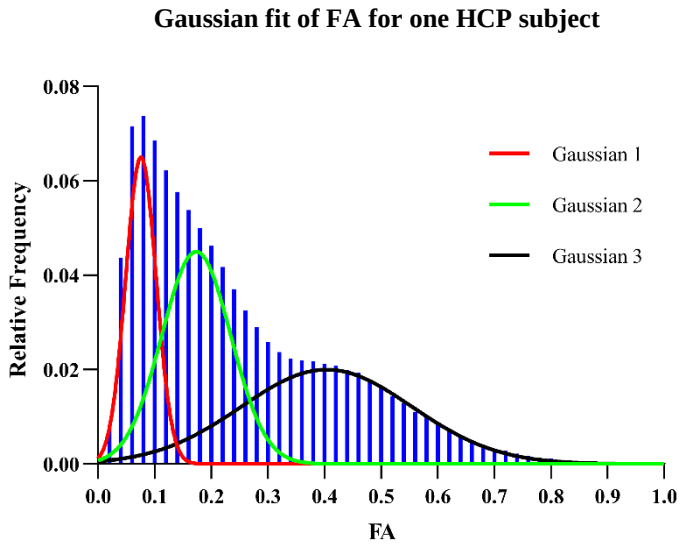

Figure 4.7: *Fit of the 3 selected gaussians to the FA histogram of one HCP subject.*

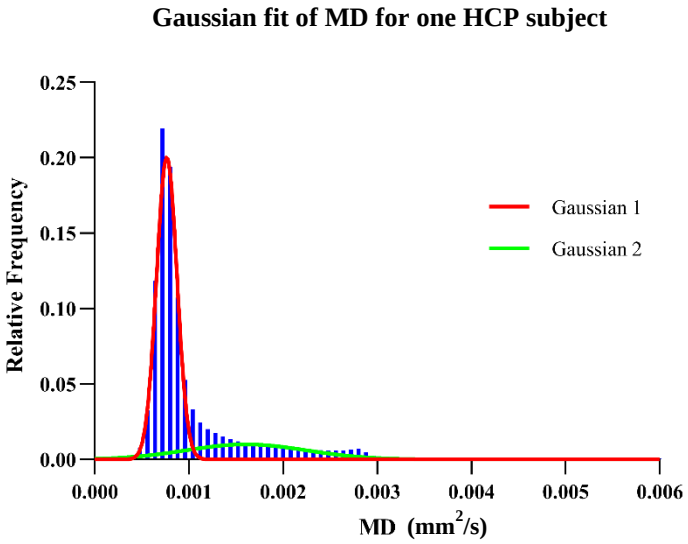

Figure 4.8: *Fit of the 2 selected gaussians to the MD histogram of one HCP subject.*

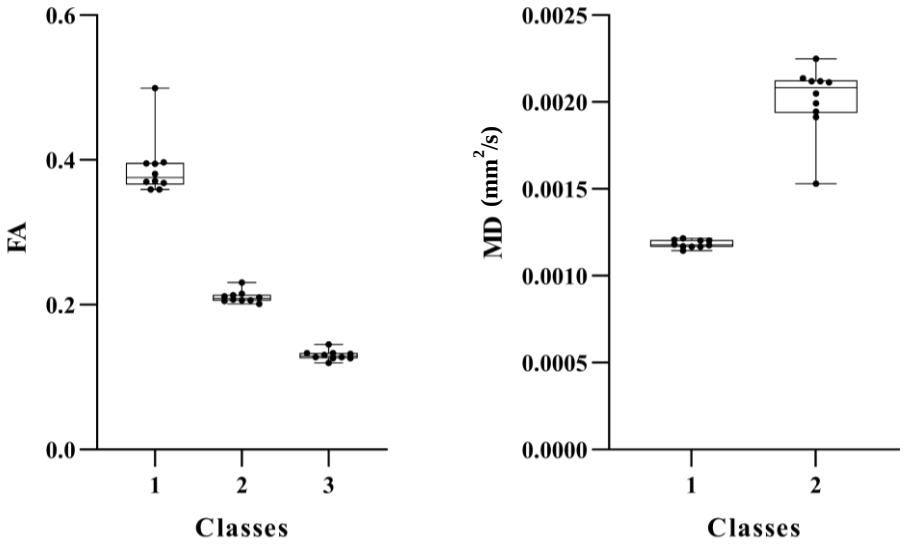

Figure 4.9: *Boxplot of FA (left) and MD (right) mean values of each class for all dHCP subjects.*

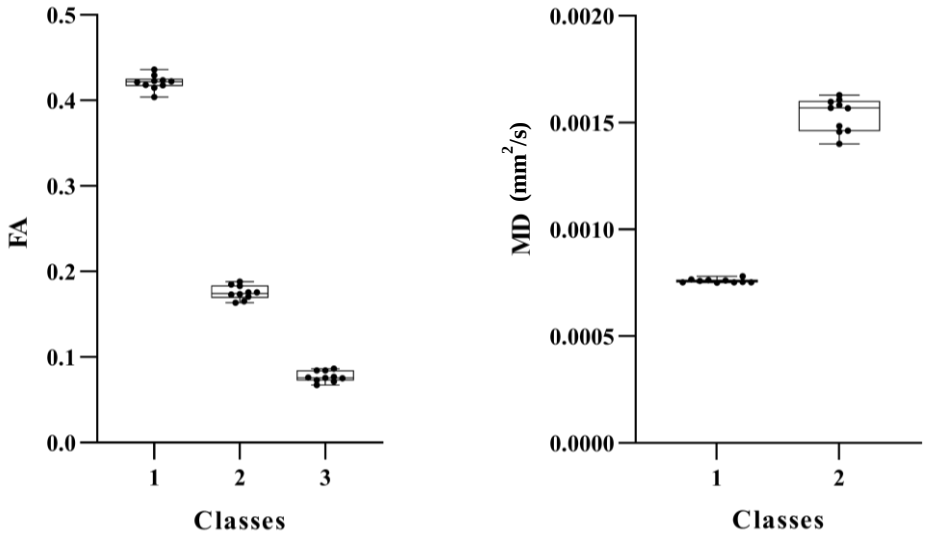

Figure 4.10: *Boxplot of FA (left) and MD (right) mean values of each class for all HCP subjects.*

4.1.3. Spatial maps

Spatial maps of the brain with the chosen final classes can be seen below. Figures 4.11 to 4.14 show the spatial maps of the dHCP data and Figures 4.15 to 4.18 show the spatial maps of the HCP data, for FA and MD. Figure 4.12 highlights the different stages of WM maturation typical of the neonatal brain. The regions colored in red (Class 1) are myelinated WM that maturates first, since these regions are responsible for the core functions of the brain and are the first to maturate, whereas the regions colored in light blue (Class 2) are non-myelinated WM, which develops later. By having two stages of WM maturation in the dHCP data, the regions colored in dark blue will correspond to two tissue types, GM and CSF (Class 3). All dHCP subjects presented very similar spatial maps (Figure 4.11).

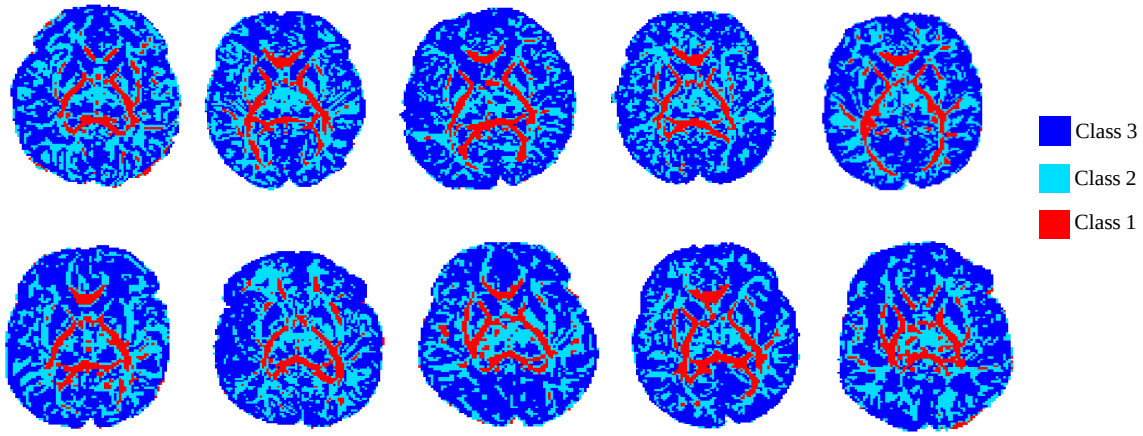

Figure 4.11: *Spatial maps of the classes derived from the FA histogram fit regarding all dHCP subjects.*

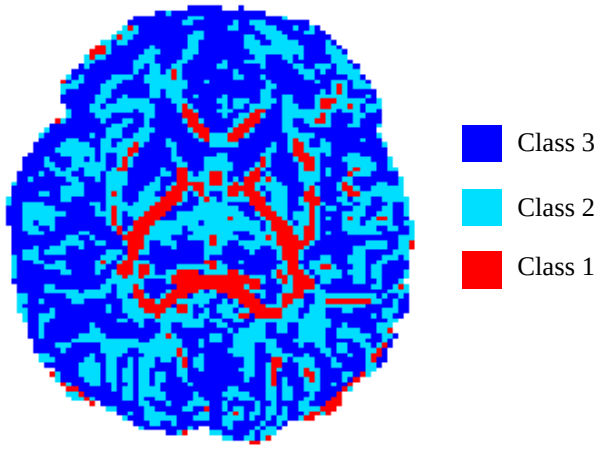

Figure 4.12: *Spatial map of the classes derived from the FA histogram fit for one dHCP subject.*

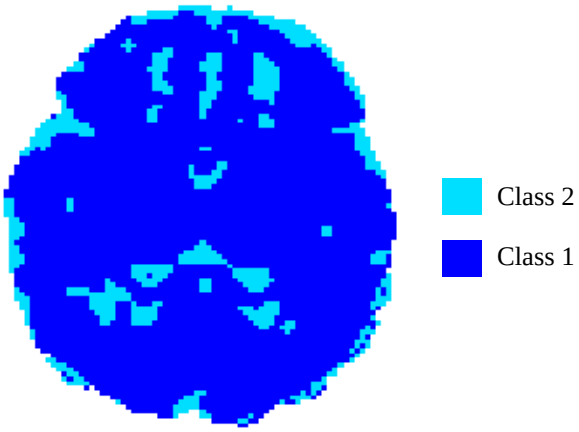

Figure 4.13: *Spatial map of the classes derived from the MD histogram fit for one dHCP subject.*

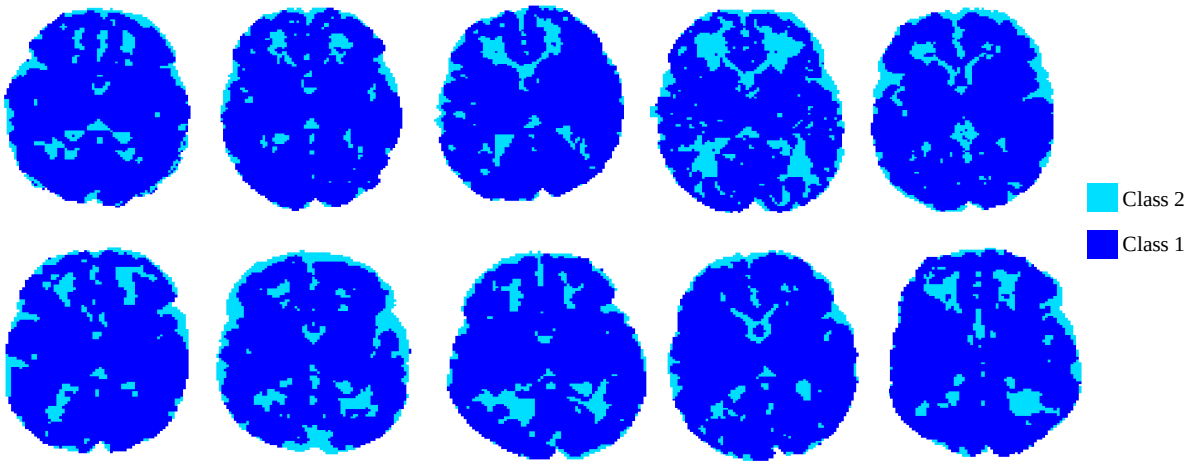

Figure 4.14: *Spatial maps of the classes derived from the MD histogram fit regarding all dHCP subjects.*

The FA spatial map of the HCP data (Figure 4.15) shows the WM in red as one single class (Class 1) since this tissue is fully maturated as would be expected. Light blue islands (Class 2) can be seen in WM regions and around the ventricles. Class 2 is likely to also be WM, whereas the dark blue regions correspond to GM and CSF. All dHCP subjects presented very similar spatial maps (Figure 4.16).

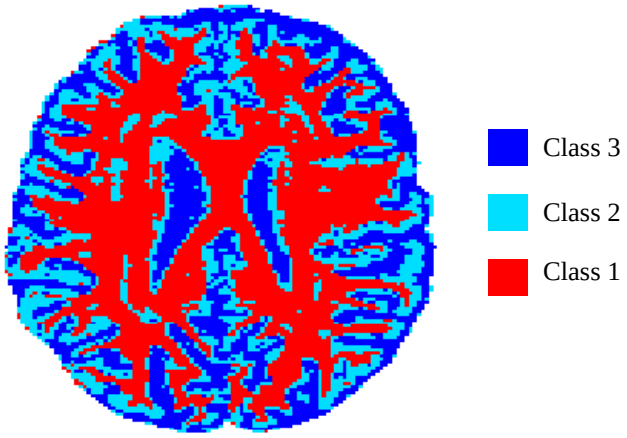

Figure 4.15: *Spatial map of the classes derived from the FA histogram fit for one HCP subject.*

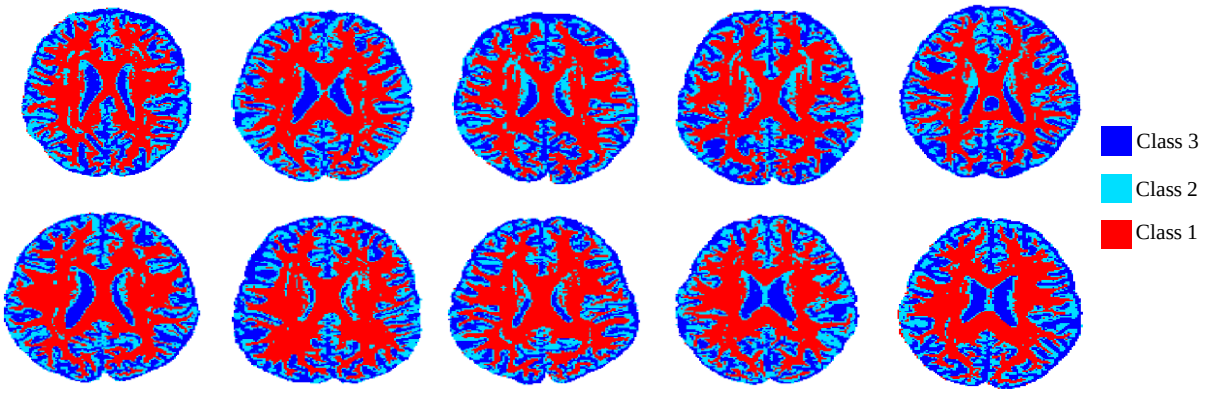

Figure 4.16: *Spatial map of the classes derived from the FA histogram fit regarding all HCP subjects.*

The MD spatial maps of both datasets (Figures 4.13 and 4.17) do not show a lot of information, since the number of defined classes for MD was two for both. The regions colored in dark blue (Class 1) correspond to WM and GM whereas the regions colored in light blue (Class 2) correspond to CSF. Both datasets showed very similar spatial maps across all subjects, as it can be seen in Figures 4.14 and 4.18. Furthermore, Figures 4.11, 4.14, 4.16, and 4.18 show that all maps make sense with anatomical correspondence.

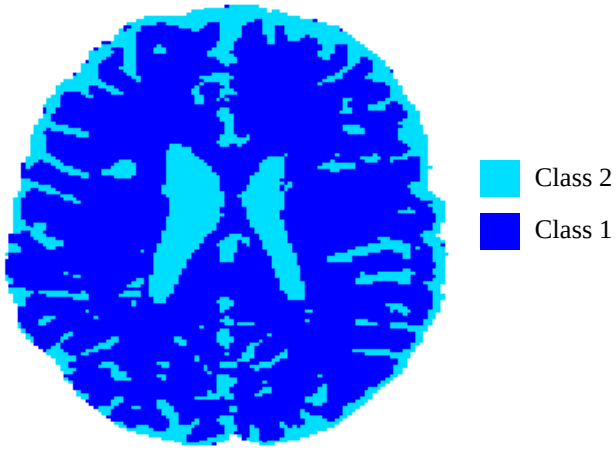

Figure 4.17: *Spatial map of the classes derived from the MD histogram fit for one HCP subject.*

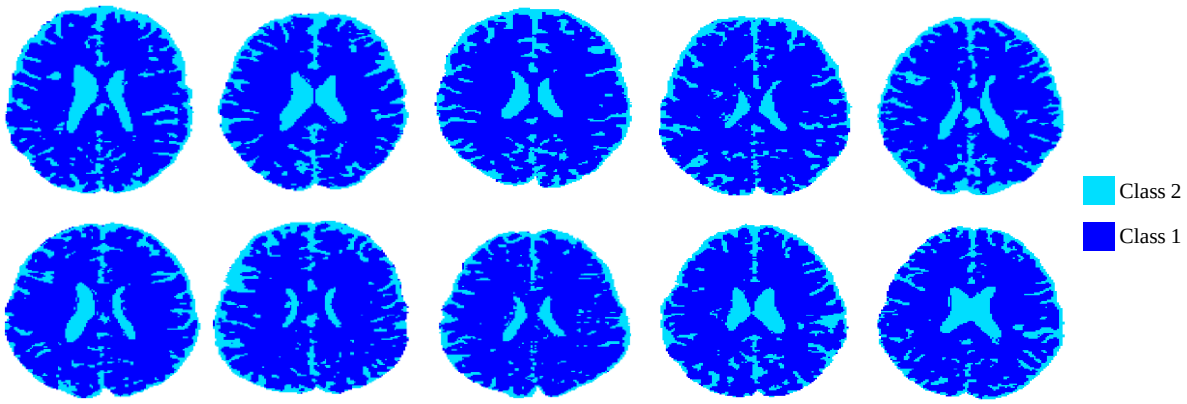

Figure 4.18: *Spatial map of the classes derived from the MD histogram fit regarding all HCP subjects.*

Figures 4.19 and 4.20 show a comparison between the spatial maps of the dHCP and HCP subjects for FA and MD, respectively. These two figures present a visual inspection of the differences between the tissue types on both datasets and how different the brain structure is in these two stages of age. The significant differences in WM regions between dHCP data and HCP data should be highlighted (Figure 4.19). Furthermore, these results demonstrate the efficiency and consistency of this automatic class selection method across all subjects.

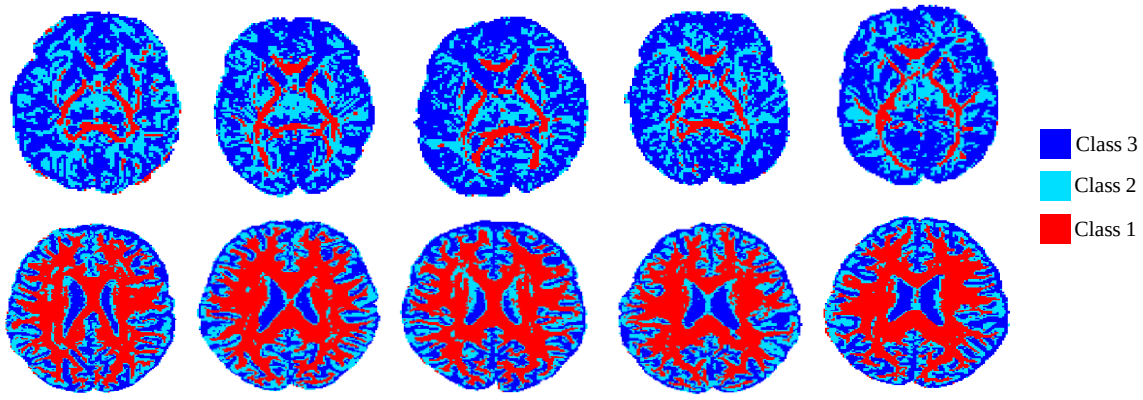

Figure 4.19: *Spatial map of the classes derived from the FA histogram fit for five dHCP subjects (top) and five HCP subjects (bottom).*

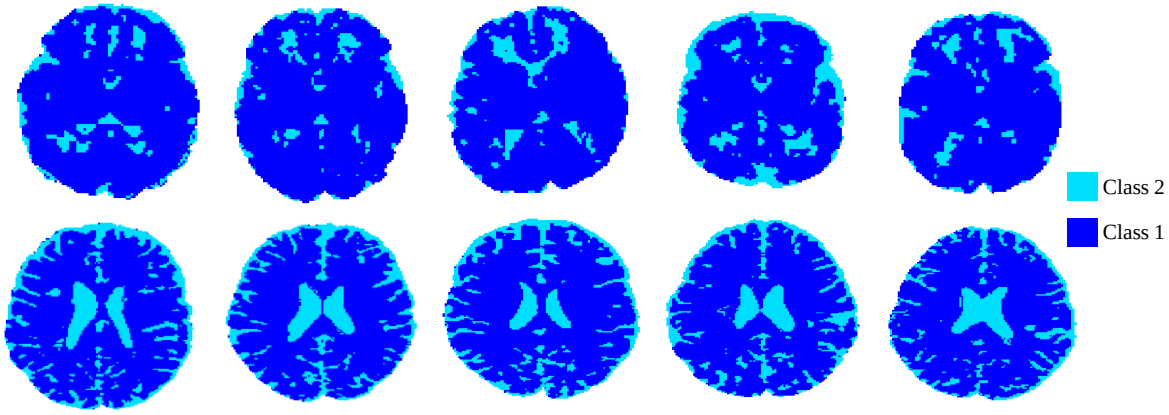

Figure 4.20: *Spatial map of the classes derived from the MD histogram fit for five dHCP subjects (top) and five HCP subjects (bottom).*

Since the ideal number of classes for FA was three and for MD was two, and each voxel is characterized by a combination of FA and MD, six classes were created, where each class corresponds to a combination of FA and MD mean values that are shown in Table 4.3. All FA and MD classes have very low standard deviation values for both datasets, demonstrating the consistency of the automatic selection of classes. Figures 4.21 and 4.22 show the brain spatial maps of both datasets using the six classes. These maps make some sense with anatomical correspondence, but some of the classes do not correspond exactly to the tissues present in the brain.

Table 4.3: *FA and MD mean values of the dHCP and HCP subjects for each class.*

	FA (Mean ± STD)			**MD x 10^{-3} (Mean ± STD) [mm^2/s]**	
	1st Class	**2nd Class**	**3rd Class**	**1st Class**	**2nd Class**
Neonates	0.39 ± 0.04	0.21 ± 0.008	0.13 ± 0.007	1.18 ± 0.02	2.02 ± 0.02
Adults	0.42 ± 0.009	0.18 ± 0.008	0.08 ± 0.006	1.00 ± 0.009	1.54 ± 0.08

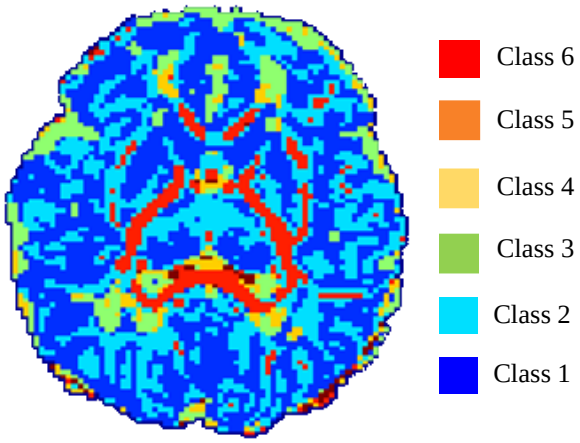

Figure 4.21: *Spatial map of the classes derived from the joint fit of the FA and MD histograms regarding all dHCP subjects.*

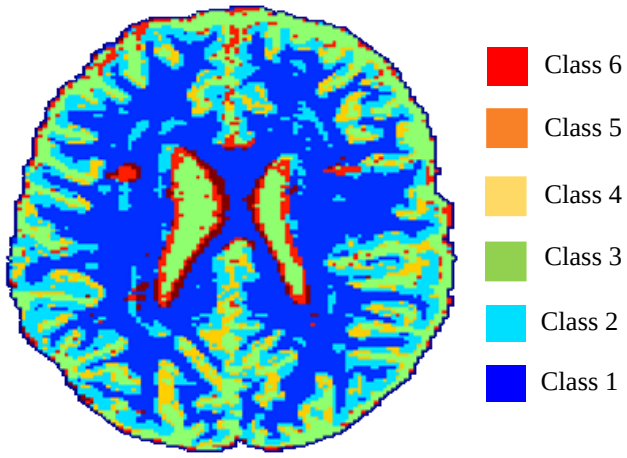

Figure 4.22: *Spatial map of the classes derived from the joint fit of the FA and MD histograms regarding all HCP subjects.*

4.2. GRL with the optimized classes

The second part of the results concerns the application of GRL using the best three combinations of classes from the six available (Figures 4.21 and 4.22), as well as a comparison between the standard GRL method and the GRL-auto method proposed in this work. As mentioned in Section 3.2.3, these classes were selected based on the frequency with which each combination occurred. Therefore, this section is divided into three parts: (1) dHCP and HCP signal fraction maps associated with the models of WM, GM, and CSF, using GRL and GRL-auto; (2) FOD representation in several brain regions of the dHCP and HCP subjects, using GRL and GRL-auto; (3) Fiber tractography maps of the neonatal and adult brains, also using GRL and GRL-auto.

4.2.1. Signal fraction maps

Figures 4.23 and 4.24 show an example of an axial slice of the signal fraction maps associated with the models of WM, GM and CSF estimated with GRL and with GRL-auto, for one HCP and one dHCP subject, respectively. The values of WM, GM, and CSF fractions were plausible and the maps were in line with the expected anatomy and looked consistent on both datasets (Figures 4.23 to 4.28). Regarding the signal fraction maps of the HCP data, it can be seen that there is almost no difference between the GRL and the GRL-auto since both methods provide very similar maps (Figure 4.23).

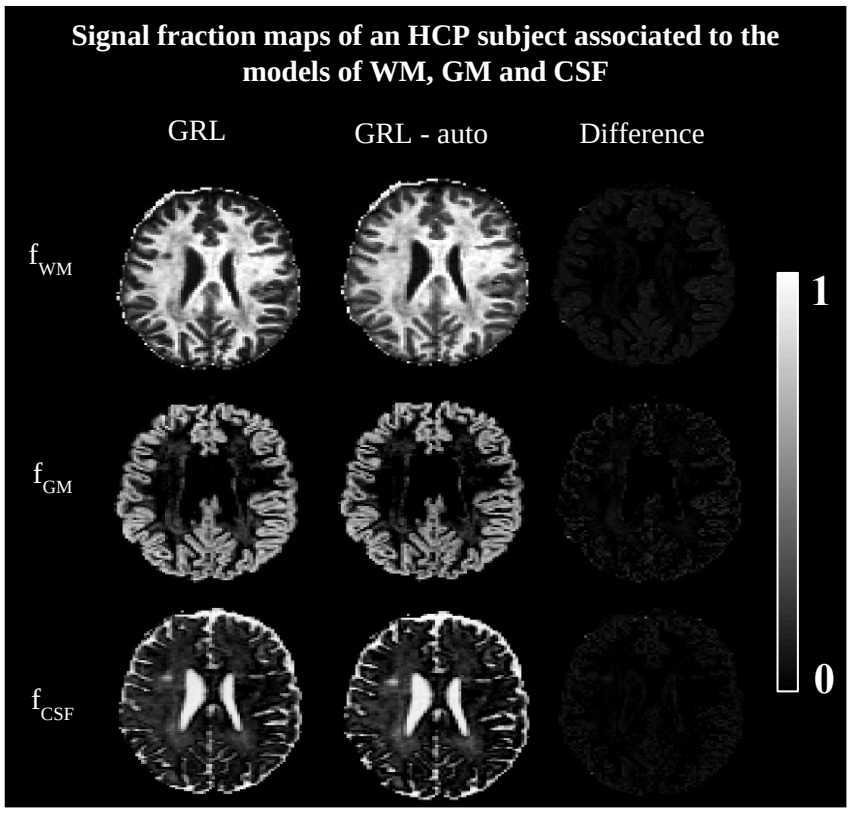

Figure 4.23: *Signal fraction maps of WM, GM and CSF estimated with GRL and GRL - auto, for one HCP subject.*

In the dHCP signal fraction map (Figure 4.24), there are some notable differences. The CSF map presented by the GRL method is very overestimated since in some regions the values are almost one, whereas the estimation of this map with GRL-auto looks more plausible anatomically. The WM map estimated with GRL-auto looks good and similar to the one estimated with GRL. Some primary tracts like the corpus callosum and the corticospinal tract have a value of one on the map, so they are highly anisotropic. In the GM map, the contrast between WM and GM is more visible in the GRL method. The visual inspection of the neonatal GM fraction map shows that the rest of the brain has another anisotropic component in the intermediate range.

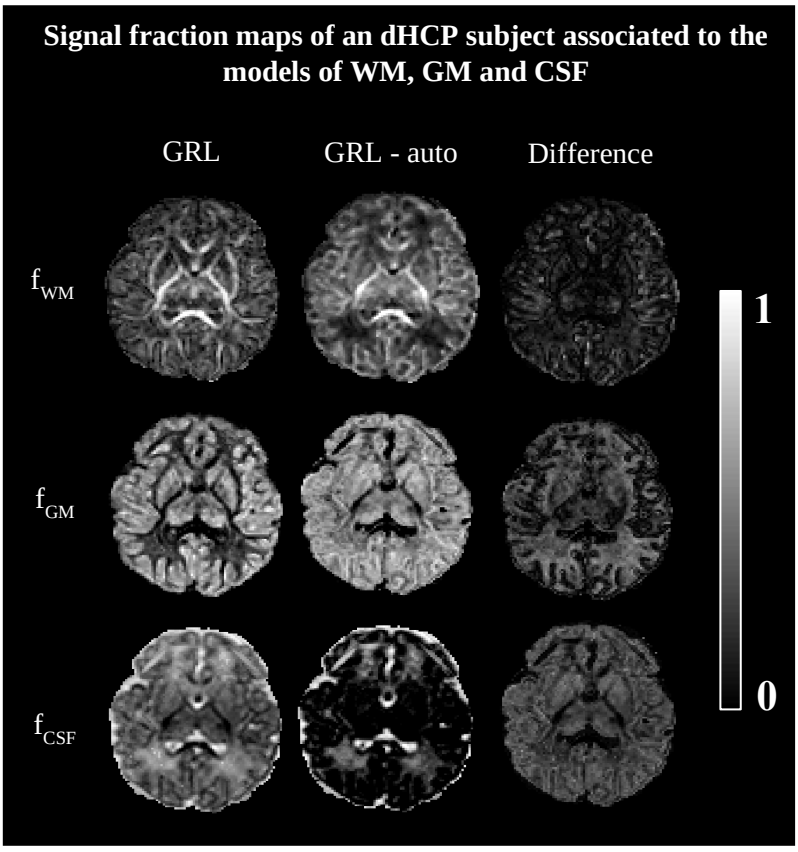

Figure 4.24: *Signal fraction maps of WM, GM and CSF estimated with GRL and GRL - auto, for one dHCP subject.*

Figures 4.25 and 4.26 show the signal fraction maps of five HCP subjects, estimated with the GRL and with GRL - auto, respectively. All maps were in line with the expected anatomy.

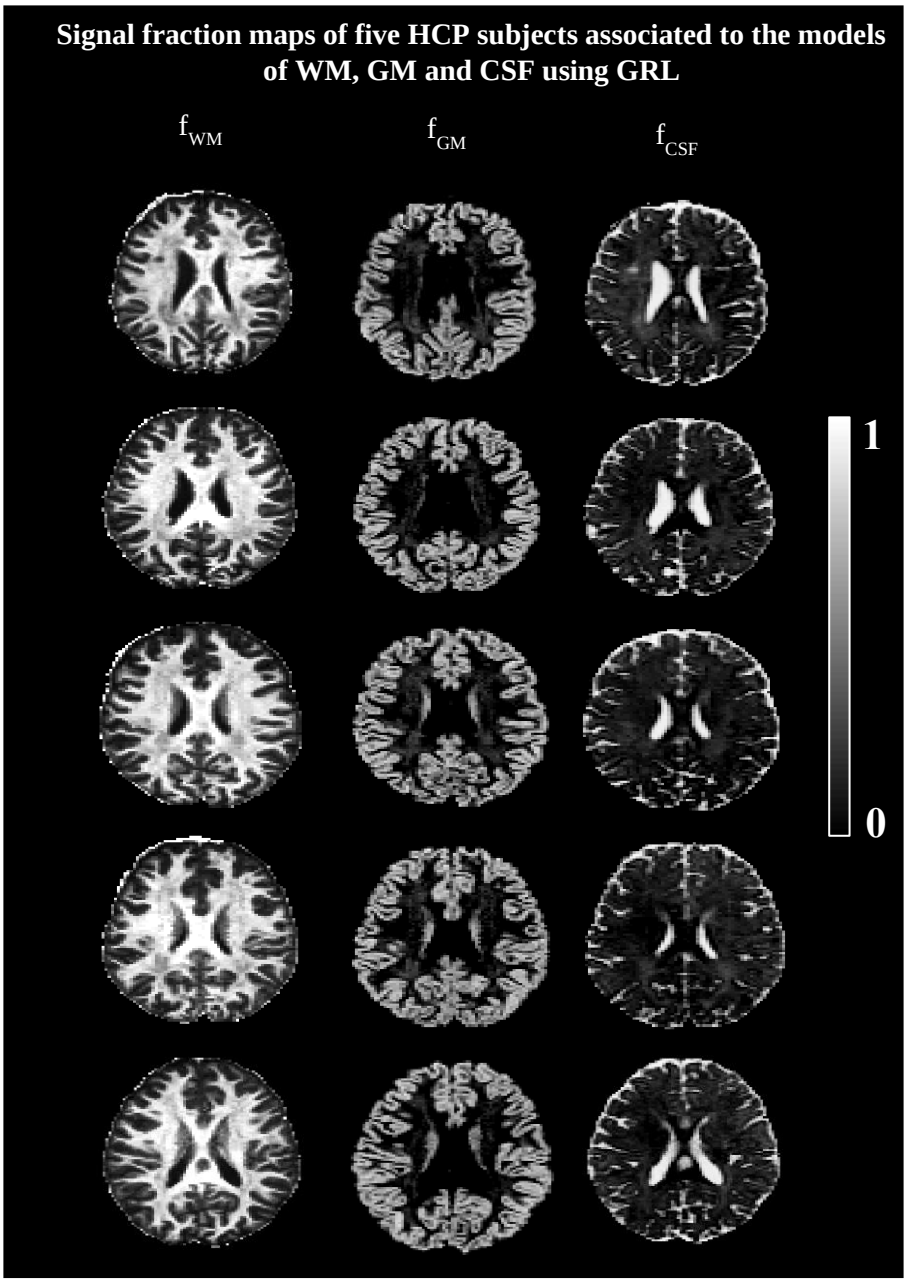

Figure 4.25: *Axial slice of the signal fraction maps of WM, GM and CSF estimated with GRL, for five HCP subjects.*

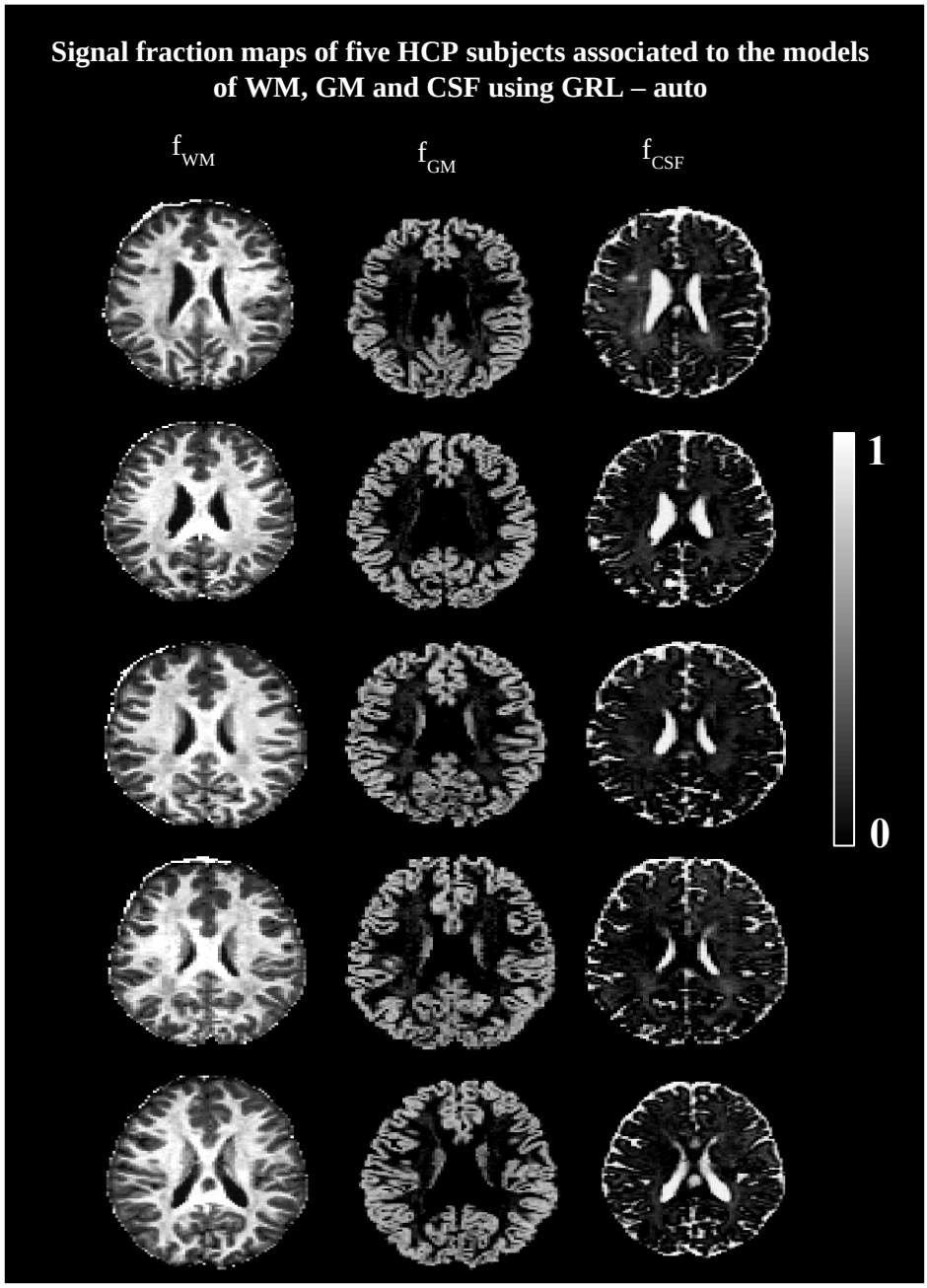

Figure 4.26: *Axial slice of the signal fraction maps of WM, GM and CSF estimated with GRL – auto, for five HCP subjects.*

Figures 4.27 and 4.28 show the signal fraction maps of five dHCP subjects, estimated with the GRL and with GRL – auto, respectively. All maps were in line with the expected anatomy.

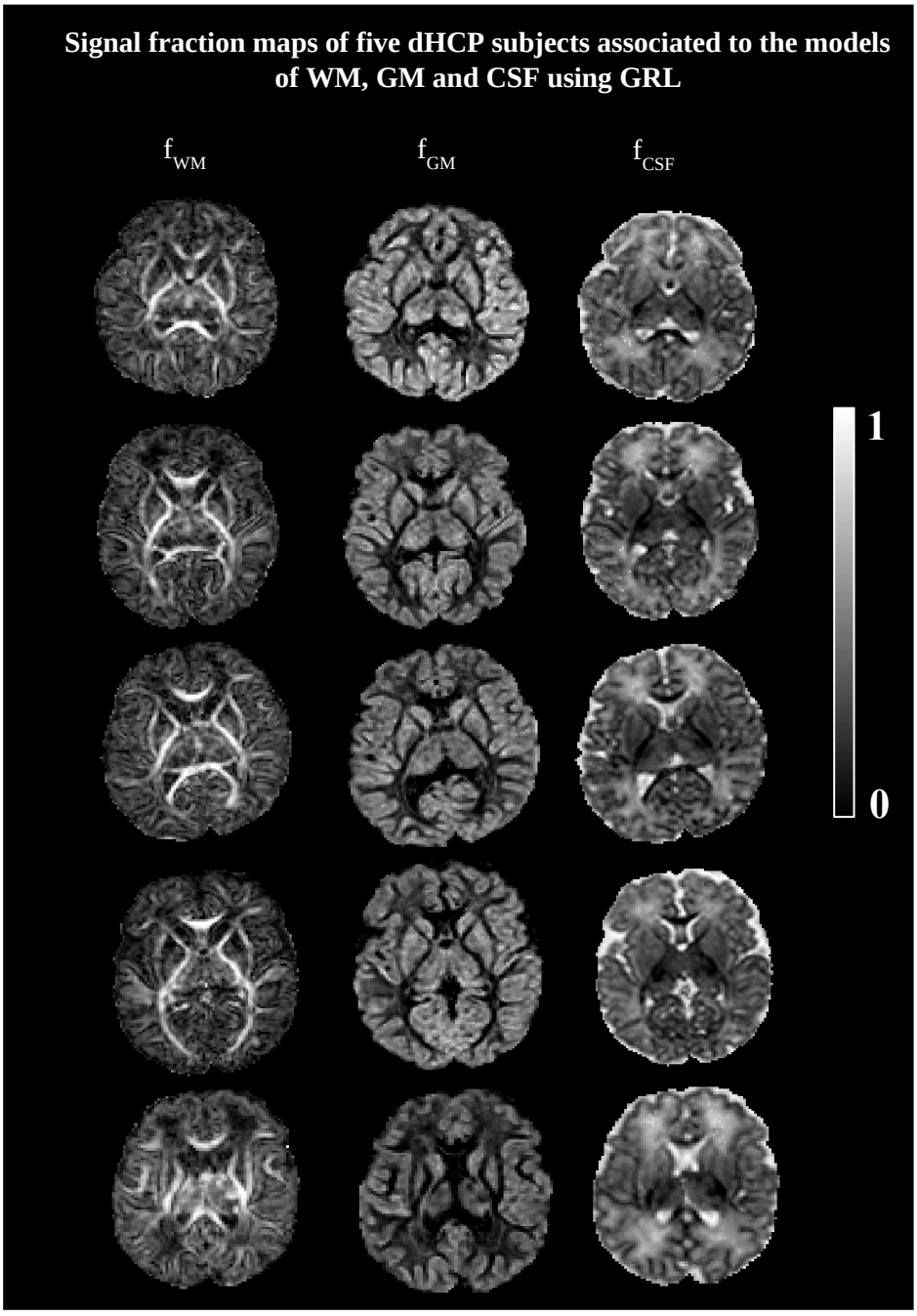

Figure 4.27: *Axial slice of the signal fraction maps of WM, GM and CSF estimated with GRL, for five dHCP subjects.*

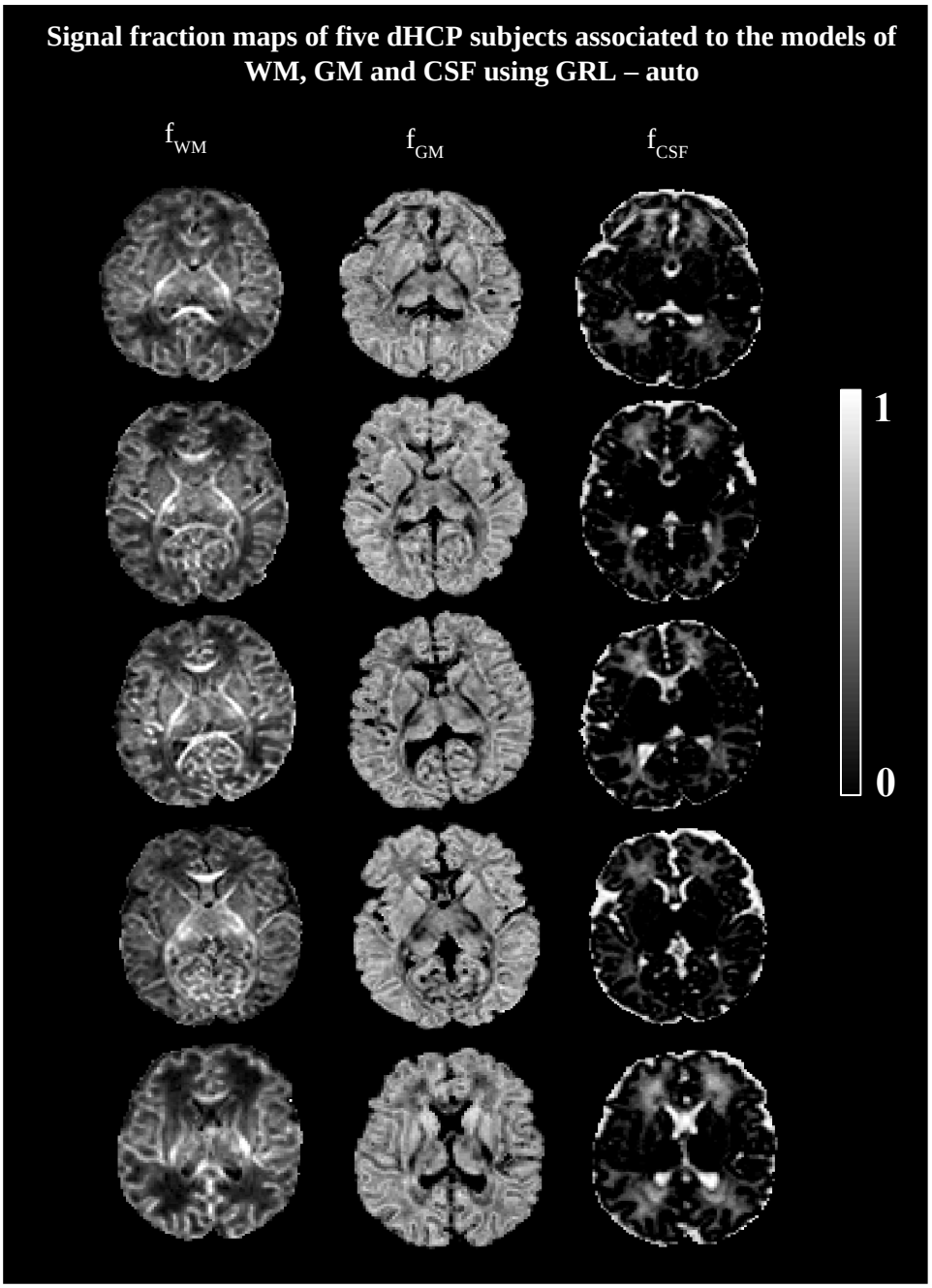

Figure 4.28: *Axial slice of the signal fraction maps of WM, GM and CSF estimated with GRL – auto, for five dHCP subjects.*

4.2.2. FOD estimation

The FODs estimated with GRL and GRL – auto for the HCP and dHCP subjects in an example coronal slice are shown in Figure 4.29.

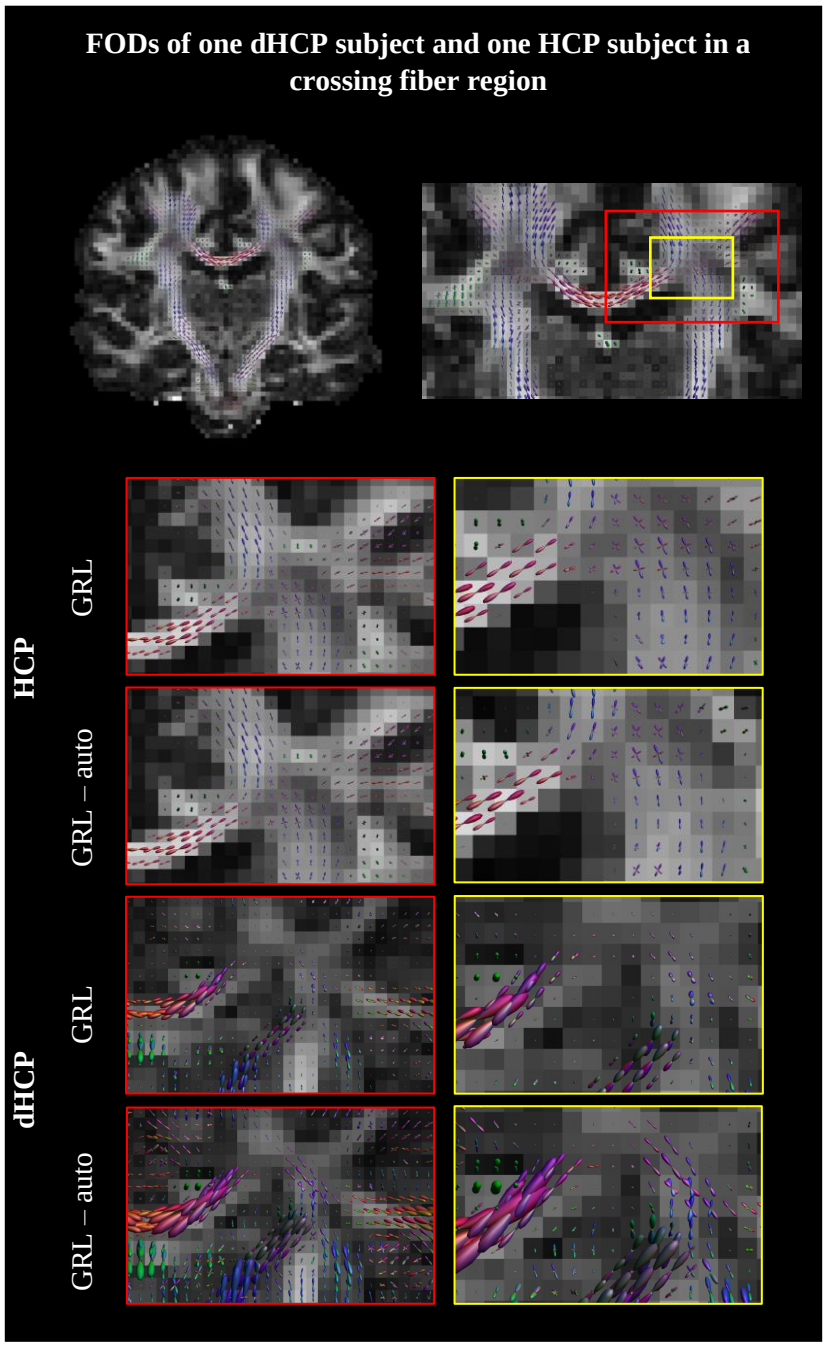

Figure 4.29: *An example coronal view of the FODs estimated with GRL and GRL - auto on one HCP and one dHCP subject with focus on the white matter of the centrum semi-ovale. Some voxels of interest where there are differences between both methods on the HCP subject are highlighted by white squares. The FODs are colored encoded according to the conventional diffusion directional color scheme.*

Regarding the HCP data FODs, there is almost no visible difference between the two methods. Nonetheless, there are some voxels highlighted by white boxes where a few differences between the two methods can be noticed.

Figure 4.30 shows the FODs estimated with GRL and GRL-auto in a crossing fiber region for one dHCP subject. In the zoomed FODs (yellow box) estimated with GRL-auto, there are some white boxes and circles highlighting some voxels of interest. GRL-auto performs better than GRL, providing excellent separation of up to three crossing fiber configurations. Furthermore, in GRL-auto it is visible that the white circle above represents a FOD that is part of the cingulum bundle, which does not have the same level of fiber separation as in the GRL method. It can also be noticed that the white circle below shows a FOD that is part of the corpus callosum and is aligned with its direction, which cannot be seen in the same voxel in the GRL. More interesting are both white boxes, where multiple voxels containing a crossing fiber representation are highlighted.

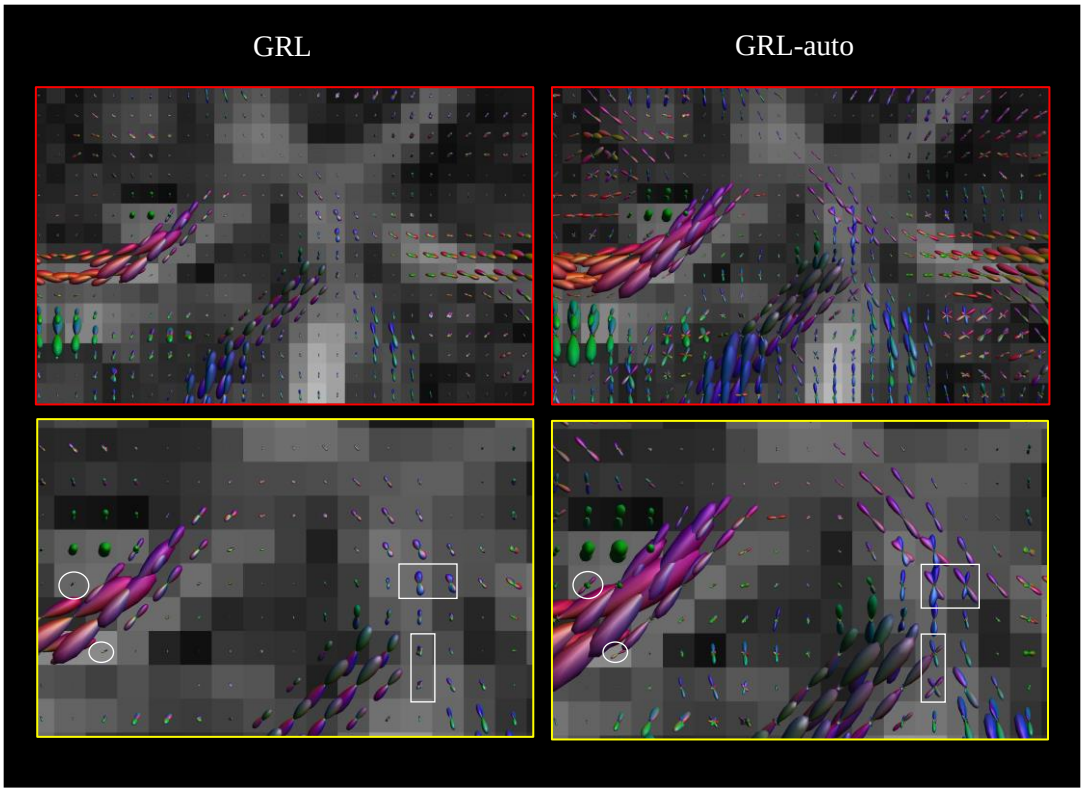

***Figure 4.30**: FODs estimated with GRL and GRL - auto on one dHCP subject with focus on some voxels that show crossing fiber separation (white circles and boxes). The FODs are colored encoded according to the conventional diffusion directional color scheme.*

The spatial maps and the histograms regarding the number of peaks detected in the FODs for GRL and GRL-auto are shown in Figure 4.31 and Figure 4.32 for the HCP and dHCP data, respectively. Regarding the HCP data, both methods give very similar spatial maps and consequently similar histograms. We noticed that the most frequent angle difference detected between both methods is zero degrees. Nonetheless, the histogram of GRL-auto shows a slight improvement in the number of three or more peaks detected. We can also observe that, on both methods, the number of peaks is mostly one in GM regions and around the ventricles, two in WM regions, and three or more in WM regions where there are more crossing fibers.

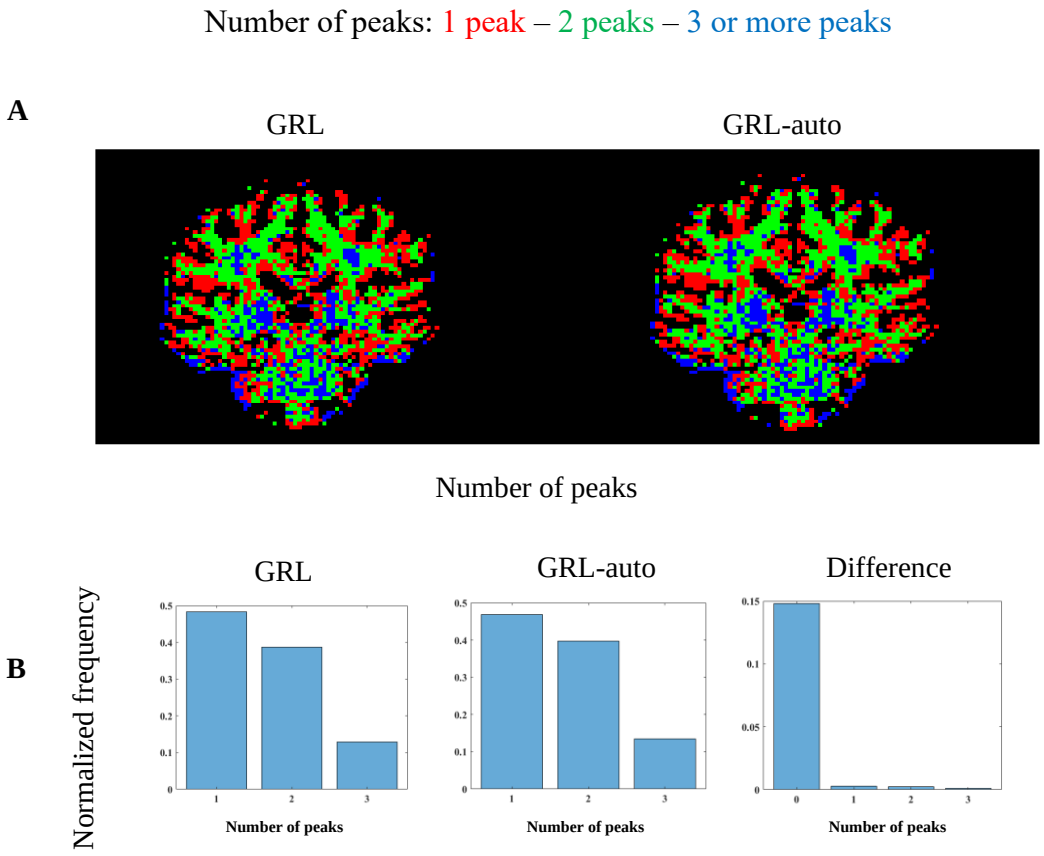

Figure 4.31: *Number of peaks detected in the FODs computed with GRL and GRL-auto on the HCP data. A) An example coronal slice showing the number of detected peaks; B) Peak frequency in the adult brain.*

Regarding the dHCP data, the number of detected peaks increased from the GRL to the GRL-auto method. The GRL-auto estimated two and three or more peaks in more crossing fiber regions of WM when compared to GRL, while estimating fewer voxels where there was only one peak detected.

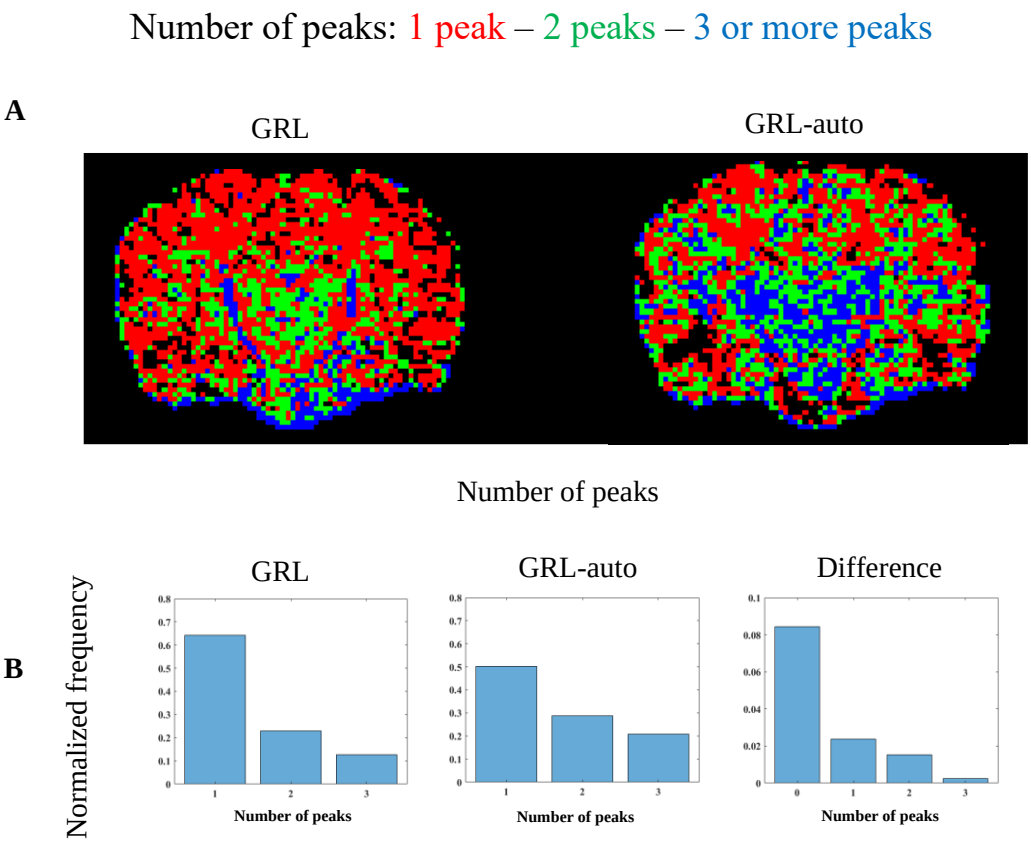

Figure 4.32: *Number of peaks detected in the FODs computed with GRL and GRL-auto on the dHCP data. A) An example coronal slice showing the number of detected peaks; B) Peak frequency in the neonatal brain.*

The frequency distribution of the angle difference between the same FOD peak estimated with GRL-auto and GRL for the HCP and dHCP data are represented in Figure 4.33 and Figure 4.34, respectively. The histogram regarding the HCP data showed almost no difference between both methods since the value of angular difference with the highest frequency of occurrence is zero degrees and most values were between 0º and 0.5º.

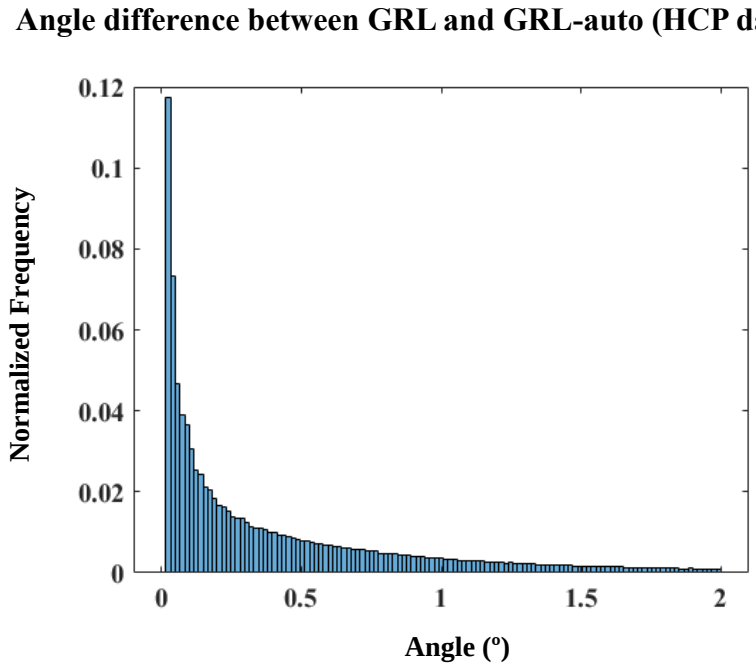

Figure 4.33: *Frequency distribution of the angle between FODs estimated with GRL and GRL-auto in the adult brain.*

Figure 4.34 show that on the dHCP data there is a significant angular difference between the main FOD peak estimated with GRL and GRL-auto. We can see that the most frequent angular differences are between 2º and 5º, even going up to 10º/15º.

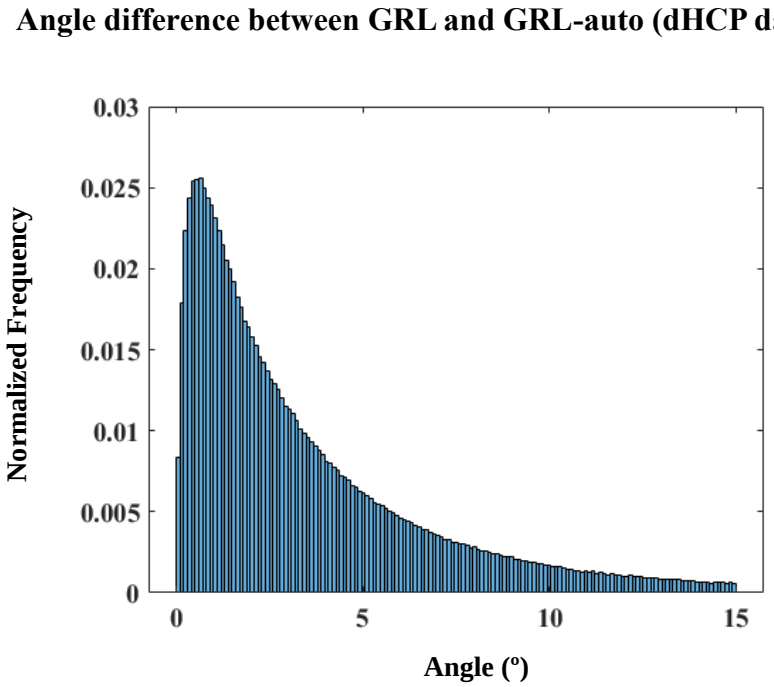

Figure 4.34*: Frequency distribution of the angle between FODs estimated with GRL and GRL-auto in the neonatal brain.*

4.2.3. Tractography

Given the fact that GRL is an already established method for fiber tractography on adult data, here we focused on the more challenging neonatal data from the dHCP. Thus, tractography was not performed in the HCP data. After the FOD estimation, fiber tractography generally requires the definition of termination criteria, such as a threshold on the amplitude of the FODs [26]. In this work, the FOD threshold amplitude was set to 0.1 on GRL and 0.3 on GRL-auto, the same as the peak threshold of the FOD. Figures 4.35 and 4.36 show the tractography results on the dHCP data in a coronal and sagittal view, respectively. It can be seen that GRL-auto introduces quite some extra spurious fibers but also reconstructs much more genuine fibers, including the left and right projections of the *corpus callosum* in the pre-central gyrus mainly visible on the right side of Figures 4.35 and 4.36, which are not visible with GRL (left side).

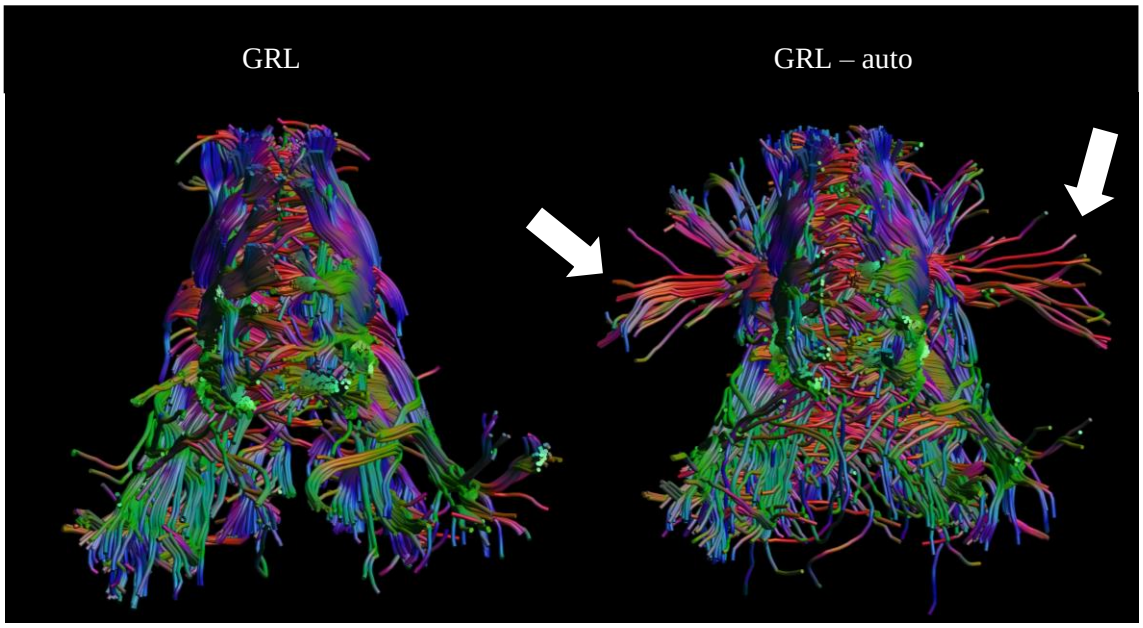

Figure 4.35: *Coronal view of neonatal brain tractography estimated with GRL (left) and GRL-auto (right). The white arrows highlight the left and right projections only visible with GRL-auto.*

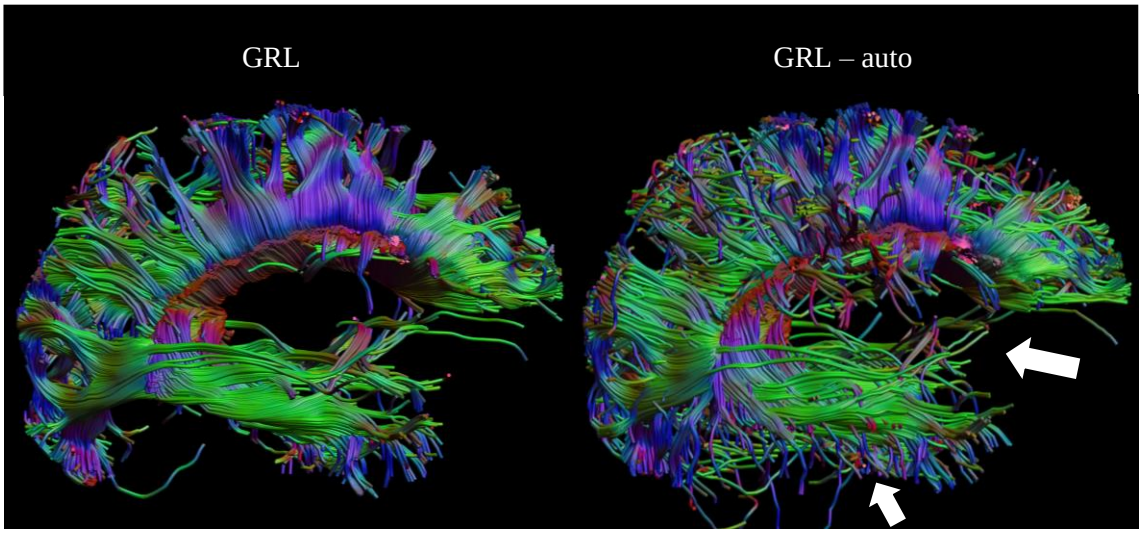

Figure 4.36: *Sagittal view of neonatal brain tractography estimated with GRL (left) and GRL-auto (right). The white arrows highlight some WM bundles only visible with GRL-auto.*

5. Discussion

In this study, a new method is developed to adaptively account for PVE in SD, by automatically selecting the number of tissue types that are needed to properly perform GRL in a brain. The complex tissue organization of the brain has led to the consideration of multiple tissues in SD methods. Furthermore, it is inappropriate to assume the properties of different tissue types to be identical between subjects throughout the whole brain since this can lead to spurious FOD reconstructions and bad performance during fiber tractography. The method here presented was named "GRL-auto" and allows the modeling of multiple tissue types and automatically defines the RF of each tissue type based on FA and MD values. By accounting for multiple tissues, properties of GM and CSF can be captured, and PVE reduced. Our results demonstrated that the method developed in this study can efficiently determine the number of tissue types needed to perform GRL in a brain, based on their FA and MD values, and ultimately improve the quality of the FOD estimation and fiber tractography.

Previously, J. D. Tournier *et al.* [8] introduced the CSD framework, a method that improves the estimated fiber orientations, by adding a non-negativity constraint on the presence of negative values in the FOD. However, this method uses the same RF for all fiber populations throughout the brain without accounting for PVE, which is not correct since the brain has a complex tissue organization made of multiple tissues. Richardson-Lucy SD was introduced by Dell'Acqua *et al.* [43] and is a method that avoids artifacts that may derive from the SH representation by extracting the FODs directly from the signal domain. Later on, Dell'Acqua *et al.* also presented the dRL framework [11] to reduce the number of spurious peaks in the FOD due to PVE. This work demonstrated the importance of accounting for the isotropic contributions of CSF in SD methods. The dRL method [11] estimates the FOD by defining a deconvolution matrix H that contains the RFs of each tissue and converting the dMRI signals into SH. However, this estimation can only be made from single-shell dMRI data, which like CSD [8] does not take into account multiple tissue classes. Jeurissen *et al.* [40] introduced the multi-shell CSD (MS-CSD) framework by applying multi-shell dMRI data on CSD and modeling particularly the contributions of GM and CSF. This showed that it is possible to improve the accuracy of the FOD estimations as compared to SD methods that only use single-shell diffusion MRI data [8], [11]. More recently, Guo *et al.* [12] used the dRL algorithm to improve the accuracy of the FOD estimation by using multi-shell dMRI data and considering multiple tissue types. This led to the GRL framework, a method that performs SD in the original signal space instead of in the SH basis [14], [30], and uses models with literature values to estimate the RFs rather than estimating them from the data, like CSD and MS-CSD [8], [40].

The method proposed in this study, addressed as GRL-auto, has several advantages when compared to the previously mentioned SD approaches. 1) This method uses multi-shell dMRI data, thus allowing the modeling of multiple tissue classes which overcomes the limitation of CSD and dRL [8], [11]; 2) Unlike CSD and MS-CSD, this method does not use SH and therefore can be used with data not distributed in shells [8], [12], [40]; 3) This method can automatically determine the number of tissue classes directly from the data, based on their FA and MD values. This makes it simple, fast, and more likely to be adapted to diverse datasets than methods relying on user input [12]; 4) Unlike some methods that only account for the three main tissue types of the brain (WM, GM, and CSF) [12], [40], GRL-auto can account for multiple tissues. This allows overcoming the inaccurate estimations that might happen if changes in the chosen tissues occur.

Our results estimated that the ideal number classes for FA was three and for MD was two (Tables 4.2 and 4.3) for both HCP and dHCP data. Furthermore, the spatial maps of the dHCP and HCP data with the applied selected classes show that in the dHCP data different stages of WM can be observed due to the

typical maturation of the neonatal brain (Figure 4.12). The regions colored in red correspond to myelinated WM that maturates first, since these regions are responsible for the core functions of the brain, whereas the regions colored in light blue are non-myelinated WM, which develops later. Therefore, from the three FA classes that were estimated in this work, two of them correspond to WM at different maturation stages in the dHCP data. This is in line with the work introduced by M. Pietsch *et al.* [69], which suggested that at least two components are required to accurately model the WM signal in neonates, leading to the use of two anisotropic RFs. By having two stages of WM maturation in the dHCP data, the regions colored in dark blue will correspond to two tissue types, GM, and CSF. This is consistent with what has been found previously [69] in adult data, where the main feature that allows the separation of different RFs is the fact that different tissue types have sufficiently distinct b-value dependencies, giving clear separation of the signal into WM, GM, and CSF. However, this separation does not occur naturally in neonates. Nonetheless, the WM signal characteristics exhibit a strong age dependence, thus allowing to observe the different maturation stages in the WM. We also described the results of the FA spatial map regarding the HCP data (Figure 4.15), which show the WM in red as one single class since this tissue is fully maturated as would be expected. The light blue islands and regions are crossing fiber regions in the WM where DTI fails, leading to the attribution of a different class. Around the ventricles, there are also some imperfections due to PVE. These results go beyond previous reports [40], showing that WM can be decomposed in two classes in adult data since in crossing fiber regions the average FA value of WM will likely be different. Furthermore, if we sum the mean FA values of class one and two of Table 4.3 regarding HCP data, we observe that it gives a total of 0.6, which is slightly below the average reported literature value of FA in all WM regarding the adult brain (0.7) [40].

The signal fractions estimated with GRL-auto on the HCP data, shown in Figure 4.23, are in line with the expected anatomy and show high correspondence to the tissue classes included in the modeling, similarly to what was previously shown with MS-CSD [40]. However, these fraction maps showed no apparent differences when compared to the standard GRL method [12]. Nonetheless, in the dHCP data, there are some notable differences. The CSF map presented by the GRL method seems overestimated given that in some regions the values are almost one (Figure 4.24). Since such amount of free water in the brain is unplausible, the CSF map estimated with GRL-auto looks more likely to reflect the underlying *in vivo* physiology and is considered as the most correct in this case. Bearing in mind that we are disentangling the truly anisotropic components, the WM map estimated with GRL-auto is in line with the one estimated with GRL. Some primary tracts like the *corpus callosum* and the corticospinal tract have a value of one on the map, which means they are highly anisotropic. Nevertheless, in the GM map, the contrast between WM and GM is more visible in the GRL method. This is in line with the work of M. Pietsch *et al.*, where it was shown that the variability in the mean signal curves between different WM structures is higher than the difference between WM and GM, which makes the separation of WM and GM more difficult [69]. The visual inspection of the neonatal GM fraction map (Figure 4.24) shows that the rest of the brain has another anisotropic component in the intermediate range, possibly because the development of the brain is still in progress. As a result, this is reflected in the GM map rather than in the CSF map.

Regarding the results of the HCP data FODs (Figure 4.29), there are very few visible differences between our method and the original formulation introduced by Guo *et al.*. When comparing our results to the previously mentioned study [12], the results regarding the number of peaks detected in the FODs of HCP data (Figure 4.31) and the angular difference between the main FOD peak (Figure 4.33) confirmed the similarity between the two methods. Although the GRL-auto method estimates the number of tissue classes automatically and defines their RFs based on the FA and MD values of each of the selected classes, in adult

data this is not sufficient to show significant differences when compared to the GRL method [12]. However, our results in the dHCP data showed that the GRL-auto performs better than the GRL, providing excellent separation of up to three crossing fiber configurations (Figure 4.30). In the proximity of the ventricles, GRL-auto visibly reduces the estimation uncertainty of the FODs and also the effect of PVE on the WM FOD, which is in line with what has already been reported in other studies [11], [12], [40]. These findings are supported by the results of the estimated number of FOD peaks (Figure 4.32) and the angular difference between the main FOD peak (Figure 4.34), demonstrating that GRL-auto can efficiently resolve multiple peaks in crossing fiber regions. However, it should be noted that after a visual inspection of the dHCP data spatial maps, we decided to use a different FOD peak threshold value than what is reported in the standard GRL method [12].

In this study, we focused on deterministic fiber tractography since it highlights the properties of the reconstructed FOD [12], [26]. GRL, alongside other studies [40], is already well established in fiber tractography on adult data [12], therefore our work focused on the more challenging neonatal data from the dHCP data. From the tractography results presented in this work (Figures 4.35 and 4.36) it is clear that, although the GRL-auto introduces quite some extra spurious fibers, it also reconstructs much more genuine fibers, such as the left and right projections of the *corpus callosum* in the pre-central gyrus, mainly visible on the right side of Figures 4.35 and 4.36, which are not visible with the standard method GRL. Overall, these results are in accordance with findings reported by other studies, which have shown that the characterization of the FOD is extremely important to get precise results in tractography [7], [12], [26], [44]–[46].

Nonetheless, this work has some limitations that should be acknowledged. Since the automatic detection of the number of tissues is based on the DTI model, it requires the acquisition of a DTI shell, which is not always done for tractography [12], [40]. Furthermore, despite being able to model and define multiple classes, this study has the constraint of a maximum number of three classes. The choice of three classes was dictated by the conventional choice in the field to represent only the three main tissues of the brain (WM, GM, and CSF). The definition of more classes might be useful, especially in presence of a disease affecting the brain non homogeneously, eventually leading to the need for a fourth "pathologic" tissue type. For simplicity, in this GRL extension, we have only accounted for one anisotropic class and N isotropic classes. Ideally, this work could eventually foster multiple anisotropic classes like the work of M. Pietsch *et al.* [69], or of De Luca *et al.* [84], allowing the investigation of differences in different WM structures.

In summary, the presented method showed good performance and consistency on both adult and neonatal dMRI datasets regarding the automatic selection of the number of tissue types that are needed to properly perform GRL in a brain, based on their FA and MD values. Furthermore, this method improved the FOD estimation by better resolving crossing fiber regions and a significant angular difference between the main FOD peaks when compared to GRL. Finally, this method demonstrated improvement in fiber tracking which can ultimately lead to a better understanding of the human brain and its development, especially if applied in neonates.

6. Conclusion

Over the last years, the development of the human brain has been studied, mostly through fiber tractography, a technique that allows the reconstruction of WM bundles that connect different brain regions, thus allowing the study of brain connectivity using dMRI data. In this study, we developed a method that automatically determines the number of tissue types that are needed to properly perform CSD in a brain, based on their FA and MD values, given multi-shell dMRI data.

Our results showed efficiency regarding the automatic selection of the number of tissue types, as well as consistency on both dHCP and HCP data. We have shown that, in neonates, this method can disentangle signal fractions from multiple tissue components, such as WM, GM, and CSF. Besides the angular resolution, identifying the correct number of peaks is crucial when estimating the number of FODs. When PVE become prominent as, for example, around the ventricles, this method estimated high-quality FODs in WM by reducing the number of spurious peaks and estimating more FOD peaks in crossing fiber regions, as compared to standard methods. All these results led to an improvement in the tractography of the neonatal brain, resulting in more plausible fiber orientations which can lead to a better understanding of the human brain and its development, which was ultimately the main goal.

This method has the advantage of being automatic, simple, fast, and is more likely to scale better to diverse datasets than methods relying on user input. This seems to be the case in the dHCP data, where a better separation of crossing fibers is achieved.

This study has shown that it can contribute to the improvement of tractography and potentially to a better study of the brain, including its maturation and connectivity. Taking into account more tissue classes, this method could open new possibilities to study brain disease since it has the potential to consider the "pathologic" class, and thus improve the analysis of data regarding patients with brain lesions.

7. References

[1] Le Bihan, D., Mangin, J. F., Poupon, C., Clark, C. A., Pappata, S., Molko, N., & Chabriat, H. (2001). Diffusion tensor imaging: concepts and applications. *Journal of magnetic resonance imaging* : JMRI, 13(4), pp. 534–546.

[2] Farquharson, S., Tournier, J. D., Calamante, F., Fabinyi, G., Schneider-Kolsky, M. E., Jackson, G., & Connelly, A. (2013). White matter fiber tractography: why we need to move beyond DTI. *Journal of Neurosurgery*, 118(6), pp. 1367 - 1377.

[3] Mori, S., & Tournier, J. D. (2013). Introduction to diffusion tensor imaging: And higher order models: Second edition. *Elsevier Inc*.

[4] Alexander, D. C., Barker, G. J., & Arridge, S. R. (2002). Detection and modeling of non-Gaussian apparent diffusion coefficient profiles in human brain data. *Magnetic resonance in medicine*, 48(2), pp. 331–340.

[5] Jeurissen, L. (2013). Investigating the prevalence of complex fiber configurations in white matter tissue with diffusion magnetic resonance imaging. *Human Brain Mapping*, 34(11), pp. 2747–2766.

[6] Basser, P. J., Mattiello, J., & LeBihan, D. (1994). Estimation of the effective self-diffusion tensor from the NMR spin echo. *Journal of magnetic resonance*. Series B, 103(3), pp. 247–254.

[7] Basser, P. J., Pajevic, S., Pierpaoli, C., Duda, J., & Aldroubi, A. (2000). In vivo fiber tractography using DT-MRI data. *Magnetic resonance in medicine*, 44(4), pp. 625–632.

[8] Tournier, J-D., Calamante, F., & Connelly, A. (2007). Robust determination of the fibre orientation distribution in diffusion MRI: Non-negativity constrained super-resolved spherical deconvolution. *NeuroImage*, 35(4), pp. 1459-1472.

[9] Behrens, T. E., Woolrich, M. W., Jenkinson, M., Johansen-Berg, H., Nunes, R. G., Clare, S., Matthews, P. M., Brady, J. M., & Smith, S. M. (2003). Characterization and propagation of uncertainty in diffusion-weighted MR imaging. *Magnetic resonance in medicine*, 50(5), pp. 1077–1088.

[10] Parker, G. J., & Alexander, D. C. (2005). Probabilistic anatomical connectivity derived from the microscopic persistent angular structure of cerebral tissue. *Philosophical transactions of the Royal Society of London. Series B, Biological sciences*, *360*(1457), pp. 893–902.

[11] Dell'acqua, F., Scifo, P., Rizzo, G., Catani, M., Simmons, A., Scotti, G., & Fazio, F. (2010). A modified damped Richardson-Lucy algorithm to reduce isotropic background effects in spherical deconvolution. *NeuroImage*, *49*(2), pp. 1446–1458.

[12] Guo, F., Leemans, A., Viergever, M. A., Dell'Acqua, F., & De Luca, A. (2020). Generalized Richardson-Lucy (GRL) for analyzing multi-shell diffusion MRI data. *NeuroImage*, *218*, 116948.

[13] Brosseau, J. (2014, April). Techniques for evaluating and improving the operational efficiency of positive train control braking enforcement algorithms. In *ASME/IEEE Joint Rail Conference* (Vol. 45356, p. V001T03A013). American Society of Mechanical Engineers.

[14] Brown, R. W., Cheng, Y. C. N., Haacke, E. M., Thompson, M. R., & Venkatesan, R. (2014). *Magnetic resonance imaging: physical principles and sequence design*. John Wiley & Sons.

[15] Winston, G. P. (2012). The physical and biological basis of quantitative parameters derived from diffusion MRI. *Quantitative imaging in medicine and surgery*, *2*(4), pp. 254–265.

[16] Assaf, Y., & Cohen, Y. (2000). Assignment of the water slow-diffusing component in the central nervous system using q-space diffusion MRS: implications for fiber tract imaging. *Magnetic resonance in medicine*, 43(2), pp. 191–199.

[17] Stejskal, E. O., & Tanner, J. E. (1965). Spin diffusion measurements: spin echoes in the presence of a time-dependent field gradient. *The journal of chemical physics*, *42*(1), pp. 288-292.

[18] Alexander, A. L., Lee, J. E., Lazar, M., & Field, A. S. (2007). Diffusion tensor imaging of the brain. *Neurotherapeutics: the journal of the American Society for Experimental NeuroTherapeutics*, *4*(3), pp. 316–329.

[19] Hagmann, P., Jonasson, L., Maeder, P., Thiran, J. P., Wedeen, V. J., & Meuli, R. (2006). Understanding diffusion MR imaging techniques: from scalar diffusion-weighted imaging to diffusion tensor imaging and beyond. *Radiographics : a review publication of the Radiological Society of North America, Inc*, *26 Suppl 1*, S205–S223.

[20] Basser, P. J., Mattiello, J., & LeBihan, D. (1994). MR diffusion tensor spectroscopy and imaging. *Biophysical journal*, *66*(1), pp. 259–267.

[21] Basser, P. J., & Pierpaoli, C. (1996). Microstructural and physiological features of tissues elucidated by quantitative-diffusion-tensor MRI. *Journal of magnetic resonance. Series B*, *111*(3), pp. 209–219.

[22] Wilkinson, M., Wang, R., van der Kouwe, A., & Takahashi, E. (2016). White and gray matter fiber pathways in autism spectrum disorder revealed by ex vivo diffusion MR tractography. *Brain and behavior*, *6*(7), pp. 1–12.

[23] Behrens, T.E.J. & Jbabdi, Saad. (2013). Diffusion MRI: from Quantitative Measurement to in vivo Neuroanatomy. *MR Diffusion Tractography*. pp. 333-351.

[24] Jones, D. K. (2004). The effect of gradient sampling schemes on measures derived from diffusion tensor MRI: a Monte Carlo study. *Magnetic Resonance in Medicine: An Official Journal of the International Society for Magnetic Resonance in Medicine*, *51*(4), pp. 807-815.

[25] Soares, J. M., Marques, P., Alves, V., & Sousa, N. (2013). A hitchhiker's guide to diffusion tensor imaging. *Frontiers in neuroscience*, *7*, 31.

[26] Behrens, T. E., Berg, H. J., Jbabdi, S., Rushworth, M. F., & Woolrich, M. W. (2007). Probabilistic diffusion tractography with multiple fibre orientations: What can we gain?. *Neuroimage*, *34*(1), pp. 144-155.

[27] Pierpaoli, C., Barnett, A., Pajevic, S., Chen, R., Penix, L. R., Virta, A., & Basser, P. (2001). Water diffusion changes in Wallerian degeneration and their dependence on white matter architecture. *NeuroImage*, 13(6 Pt 1), pp. 1174–1185.

[28] Dell'Acqua, F., & Tournier, J. D. (2019). Modelling white matter with spherical deconvolution: How and why?. *NMR in Biomedicine*, *32*(4), e3945., pp. 1–18.

[29] Healy Jr, D. M., Hendriks, H., & Kim, P. T. (1998). Spherical deconvolution. *Journal of Multivariate Analysis*, *67*(1), pp. 1-22.

[30] Tournier, J. D., Calamante, F., Gadian, D. G., & Connelly, A. (2004). Direct estimation of the fiber orientation density function from diffusion-weighted MRI data using spherical deconvolution. *Neuroimage*, *23*(3), pp. 1176-1185.

[31] Beaulieu, C. (2002). The basis of anisotropic water diffusion in the nervous system–a technical review. *NMR in Biomedicine: An International Journal Devoted to the Development and Application of Magnetic Resonance In Vivo*, *15*(7-8), pp. 435-455.

[32] Tournier, J. D., Yeh, C. H., Calamante, F., Cho, K. H., Connelly, A., & Lin, C. P. (2008). Resolving crossing fibres using constrained spherical deconvolution: validation using diffusion-weighted imaging phantom data. *Neuroimage*, *42*(2), pp. 617-625.

[33] Jeurissen, B., Leemans, A., Tournier, J. D., Jones, D. K., & Sijbers, J. (2010, May). Estimating the number of fiber orientations in diffusion MRI voxels: a constrained spherical deconvolution study. In *International Society for Magnetic Resonance in Medicine (ISMRM)* (p. 573).

[34] Andersson, J. L., & Sotiropoulos, S. N. (2015). Non-parametric representation and prediction of single- and multi-shell diffusion-weighted MRI data using Gaussian processes. *NeuroImage*, *122*, pp. 166–176.

[35] Andersson, J., & Sotiropoulos, S. N. (2016). An integrated approach to correction for off-resonance effects and subject movement in diffusion MR imaging. *NeuroImage*, *125*, pp. 1063–1078.

[36] Alexander, D. C., & Barker, G. J. (2005). Optimal imaging parameters for fiber-orientation estimation in diffusion MRI. *NeuroImage*, *27*(2), pp. 357–367.

[37] Mori, S., & van Zijl, P. C. (2002). Fiber tracking: principles and strategies - a technical review. *NMR in biomedicine*, *15*(7-8), pp. 468–480.

[38] Jones, D. K. (2008). Studying connections in the living human brain with diffusion MRI. *Cortex; A journal devoted to the study of the nervous system and behavior*, *44*(8), pp. 936–952.

[39] Raffelt, D., Tournier, J. D., Rose, S., Ridgway, G. R., Henderson, R., Crozier, S., Salvado, O., & Connelly, A. (2012). Apparent Fibre Density: a novel measure for the analysis of diffusion-weighted magnetic resonance images. *NeuroImage*, *59*(4), pp. 3976–3994.

[40] Jeurissen, B., Tournier, J. D., Dhollander, T., Connelly, A., & Sijbers, J. (2014). Multi-tissue constrained spherical deconvolution for improved analysis of multi-shell diffusion MRI data. *NeuroImage*, *103*, pp. 411-426.

[41] Roine, T., Jeurissen, B., Perrone, D., Aelterman, J., Leemans, A., Philips, W., & Sijbers, J. (2014). Isotropic non-white matter partial volume effects in constrained spherical deconvolution. *Frontiers in neuroinformatics*, *8*, 28.

[42] Dell'Acqua, F., Simmons, A., Williams, S. C., & Catani, M. (2013). Can spherical deconvolution provide more information than fiber orientations? Hindrance modulated orientational anisotropy, a true-tract specific index to characterize white matter diffusion. *Human brain mapping*, *34*(10), pp. 2464–2483.

[43] Dell'Acqua, F., Rizzo, G., Scifo, P., Clarke, R. A., Scotti, G., & Fazio, F. (2007). A model-based deconvolution approach to solve fiber crossing in diffusion-weighted MR imaging. *IEEE transactions on bio-medical engineering*, *54*(3), pp. 462–472.

[44] Tournier, J. D., Mori, S., & Leemans, A. (2011). Diffusion tensor imaging and beyond. *Magnetic resonance in medicine*, *65*(6), pp. 1532–1556.

[45] Conturo, T. E., Lori, N. F., Cull, T. S., Akbudak, E., Snyder, A. Z., Shimony, J. S., McKinstry, R. C., Burton, H., & Raichle, M. E. (1999). Tracking neuronal fiber pathways in the living human brain. *Proceedings of the National Academy of Sciences of the United States of America*, *96*(18), pp. 10422–10427.

[46] Tournier, J. D., Calamante, F., & Connelly, A. (2012). MRtrix: diffusion tractography in crossing fiber regions. *International journal of imaging systems and technology*, *22*(1), pp. 53-66.

[47] Budde, M. D., & Annese, J. (2013). Quantification of anisotropy and fiber orientation in human brain histological sections. Frontiers in integrative neuroscience, 7, 3.

[48] Schilling, K., Janve, V., Gao, Y., Stepniewska, I., Landman, B. A., & Anderson, A. W. (2016). Comparison of 3D orientation distribution functions measured with confocal microscopy and diffusion MRI. *NeuroImage*, *129*, pp. 185–197.

[49] Anderson, A. W. (2005). Measurement of fiber orientation distributions using high angular resolution diffusion imaging. *Magnetic resonance in medicine*, *54*(5), pp. 1194–1206.

[50] Frank, L. R. (2001). Anisotropy in high angular resolution diffusion-weighted MRI. *Magnetic resonance in medicine*, *45*(6), pp. 935–939.

[51] Descoteaux, M., Angelino, E., Fitzgibbons, S., & Deriche, R. (2007). Regularized, fast, and robust analytical Q-ball imaging. *Magnetic resonance in medicine*, *58*(3), pp. 497–510.

[52] Hess, C. P., Mukherjee, P., Han, E. T., Xu, D., & Vigneron, D. B. (2006). Q-ball reconstruction of multimodal fiber orientations using the spherical harmonic basis. *Magnetic resonance in medicine*, *56*(1), pp. 104–117.

[53] Frank, L. R. (2002). Characterization of anisotropy in high angular resolution diffusion-weighted MRI. *Magnetic resonance in medicine*, *47*(6), pp. 1083–1099.

[54] Roine, T., Jeurissen, B., Perrone, D., Aelterman, J., Philips, W., Leemans, A., & Sijbers, J. (2015). Informed constrained spherical deconvolution (iCSD). *Medical image analysis*, *24*(1), pp. 269-281.

[55] Raffelt, D. A., Tournier, J. D., Smith, R. E., Vaughan, D. N., Jackson, G., Ridgway, G. R., & Connelly, A. (2017). Investigating white matter fibre density and morphology using fixel-based analysis. *NeuroImage*, *144*(Pt A), pp. 58–73.

[56] Raffelt, D. A., Smith, R. E., Ridgway, G. R., Tournier, J. D., Vaughan, D. N., Rose, S., Henderson, R., & Connelly, A. (2015). Connectivity-based fixel enhancement: Whole-brain statistical analysis of diffusion MRI measures in the presence of crossing fibres. *NeuroImage*, *117*, pp. 40–55.

[57] Assaf, Y., & Basser, P. J. (2005). Composite hindered and restricted model of diffusion (CHARMED) MR imaging of the human brain. *NeuroImage*, *27*(1), pp. 48–58.

[58] Hosey, T. P., Harding, S. G., Carpenter, T. A., Ansorge, R. E., & Williams, G. B. (2008). Application of a probabilistic double-fibre structure model to diffusion-weighted MR images of the human brain. *Magnetic resonance imaging*, *26*(2), pp. 236–245.

[59] Sotiropoulos, S. N., Jbabdi, S., Xu, J., Andersson, J. L., Moeller, S., Auerbach, E. J., Glasser, M. F., Hernandez, M., Sapiro, G., Jenkinson, M., Feinberg, D. A., Yacoub, E., Lenglet, C., Van Essen, D. C., Ugurbil, K., Behrens, T. E., & WU-Minn HCP Consortium (2013). Advances in diffusion MRI acquisition and processing in the Human Connectome Project. *NeuroImage*, *80*, pp. 125–143.

[60] Parker, G. D., Marshall, D., Rosin, P. L., Drage, N., Richmond, S., & Jones, D. K. (2013). A pitfall in the reconstruction of fibre ODFs using spherical deconvolution of diffusion MRI data. *NeuroImage*, *65*, pp. 433–448.

[61] Descoteaux, M., Deriche, R., Knösche, T. R., & Anwander, A. (2009). Deterministic and probabilistic tractography based on complex fibre orientation distributions. *IEEE transactions on medical imaging*, *28*(2), pp. 269–286.

[62] Lampinen, B., Szczepankiewicz, F., Mårtensson, J., van Westen, D., Sundgren, P. C., & Nilsson, M. (2017). Neurite density imaging versus imaging of microscopic anisotropy in diffusion MRI: A model comparison using spherical tensor encoding. *NeuroImage*, *147*, pp. 517–531.

[63] Schultz, T., & Groeschel, S. (2013, September). Auto-calibrating spherical deconvolution based on ODF sparsity. In *International Conference on Medical Image Computing and Computer-Assisted Intervention* (pp. 663-670). Springer, Berlin, Heidelberg.

[64] Sporns, O., Tononi, G., & Kötter, R. (2005). The human connectome: A structural description of the human brain. *PLoS computational biology*, *1*(4), e42.

[65] Ghosh, A., & Deriche, R. (2013). From diffusion MRI to brain connectomics. In *Modeling in Computational Biology and Biomedicine* (pp. 193-234). Springer, Berlin, Heidelberg.

[66] Jeurissen, B., Descoteaux, M., Mori, S., & Leemans, A. (2019). Diffusion MRI fiber tractography of the brain. *NMR in Biomedicine*, *32*(4), e3785.

[67] Brody, B. A., Kinney, H. C., Kloman, A. S., & Gilles, F. H. (1987). Sequence of central nervous system myelination in human infancy. I. An autopsy study of myelination. *Journal of neuropathology and experimental neurology*, *46*(3), pp. 283–301.

[68] Dobbing, J., & Sands, J. (1973). Quantitative growth and development of human brain. *Archives of disease in childhood*, *48*(10), pp. 757–767.

[69] Pietsch, M., Christiaens, D., Hutter, J., Cordero-Grande, L., Price, A. N., Hughes, E., ... & Tournier, J. D. (2019). A framework for multi-component analysis of diffusion MRI data over the neonatal period. *NeuroImage*, *186*, pp. 321-337.

[70] Pecheva, D., Kelly, C., Kimpton, J., Bonthrone, A., Batalle, D., Zhang, H., & Counsell, S. J. (2018). Recent advances in diffusion neuroimaging: applications in the developing preterm brain. *F1000Research*, *7*, pp. 1–12.

[71] Yoshida, S., Oishi, K., Faria, A. V., & Mori, S. (2013). Diffusion tensor imaging of normal brain development. *Pediatric radiology*, *43*(1), pp. 15–27.

[72] Kaden, E., Knösche, T. R., & Anwander, A. (2007). Parametric spherical deconvolution: inferring anatomical connectivity using diffusion MR imaging. *NeuroImage*, *37*(2), pp. 474–488.

[73] Hughes, E. J., Winchman, T., Padormo, F., Teixeira, R., Wurie, J., Sharma, M., Fox, M., Hutter, J., Cordero-Grande, L., Price, A. N., Allsop, J., Bueno-Conde, J., Tusor, N., Arichi, T., Edwards, A. D., Rutherford, M. A., Counsell, S. J., & Hajnal, J. V. (2017). A dedicated neonatal brain imaging system. *Magnetic resonance in medicine*, *78*(2), pp. 794–804.

[74] Hutter, J., Tournier, J. D., Price, A. N., Cordero-Grande, L., Hughes, E. J., Malik, S., ... & Hajnal, J. V. (2018). Time-efficient and flexible design of optimized multishell HARDI diffusion. *Magnetic resonance in medicine*, *79*(3), pp. 1276-1292.

[75] Sotiropoulos, S. N., Jbabdi, S., Xu, J., Andersson, J. L., Moeller, S., Auerbach, E. J., ... & Wu-Minn Hcp Consortium. (2013). Advances in diffusion MRI acquisition and processing in the Human Connectome Project. *Neuroimage*, *80*, pp. 125-143.

[76] Caruyer, E., Lenglet, C., Sapiro, G., & Deriche, R. (2013). Design of multishell sampling schemes with uniform coverage in diffusion MRI. *Magnetic resonance in medicine*, *69*(6), pp. 1534-1540.

[77] Leemans, A. J. B. S. J. J. D. K., Jeurissen, B., Sijbers, J., & Jones, D. K. (2009, April). ExploreDTI: a graphical toolbox for processing, analyzing, and visualizing diffusion MR data. In *Proc Intl Soc Mag Reson Med* (Vol. 17, No. 1).

[78] Reynolds, D. A. (2009). Gaussian Mixture Models. *Encyclopedia of biometrics*, *741*, pp. 659-663.

[79] Neath, A. A., & Cavanaugh, J. E. (2012). The Bayesian information criterion: background, derivation, and applications. *Wiley Interdisciplinary Reviews: Computational Statistics*, *4*(2), pp. 199-203.

[80] Myung, I. J. (2003). Tutorial on maximum likelihood estimation. *Journal of mathematical Psychology*, *47*(1), pp. 90-100.

[81] Unser, M., Aldroubi, A., & Eden, M. (1993). B-spline signal processing. I. Theory. IEEE transactions on signal processing, 41(2), pp. 821-833.

[82] Unser, M., Aldroubi, A., & Eden, M. (1993). B-spline signal processing. II. Efficiency design and applications. *IEEE transactions on signal processing*, *41*(2), pp. 834-848.

[83] Ashburner, J., & Friston, K. J. (2007). Rigid body registration. *Statistical parametric mapping: The analysis of functional brain images*, pp. 49-62.

[84] De Luca, A., Guo, F., Froeling, M., & Leemans, A. (2020). Spherical deconvolution with tissue-specific response functions and multi-shell diffusion MRI to estimate multiple fiber orientation distributions (mFODs). *NeuroImage*, *222*, 117206.